RESEARCH ARTICLE | MARCH 20 2023

Roughness effect on hypersonic second mode instability and transition on a cone

Special Collection: Hypersonic Flow

Christopher Haley ; Xiaolin Zhong (钟小林)

Physics of Fluids 35, 034113 (2023)
https://doi.org/10.1063/5.0137902

Physics of Fluids ARTICLE scitation.org/journal/phf

Roughness effect on hypersonic second mode instability and transition on a cone

Cite as: Phys. Fluids **35**, 034113 (2023); doi: 10.1063/5.0137902
Submitted: 6 December 2022 · Accepted: 2 March 2023 ·
Published Online: 20 March 2023

View Online Export Citation CrossMark

Christopher Haley[a] and Xiaolin Zhong (钟小林)[b]

AFFILIATIONS

Mechanical and Aerospace Engineering Department, University of California, Los Angeles, California 90095, USA

Note: This paper is part of the special topic, Hypersonic Flow.
[a]**Author to whom correspondence should be addressed:** clhaley@g.ucla.edu
[b]**Electronic mail:** xiaolin@seas.ucla.edu

ABSTRACT

Recent studies by Fong *et al.* ["Finite roughness effect on modal growth of a hypersonic boundary layer," AIAA Paper No. 2012-1086, 2012; "Stabilization of hypersonic boundary layer waves using 2-D surface roughness," AIAA Paper No. 2013-2985, 2013; "Numerical simulation of roughness effect on the stability of a hypersonic boundary layer," Comput. Fluids **96**, 350–367 (2014); and "Second mode suppression in hypersonic boundary layer by roughness: Design and experiments," AIAA J. **53**, 1–6 (2015)] have shown that finite roughness can attenuate Mack's second mode instability when placed at the discrete mode synchronization location for two-dimensional planar flow over a flat plate. However, more practical hypersonic flows are non-planer conical flows, and the roughness effect phenomenon in conical flows has not been extensively investigated. For that reason, this investigation research the ability of finite roughness strips to attenuate the second mode instability on a Mach 8 straight blunt cone with a freestream unit Reynolds number of 9 585 000. Two roughness configurations are studied: a single roughness strip and an array of six sequential strips. N-factor calculations determine the second mode frequency most likely to lead to turbulent transition, and the linear stability theory is used to determine the mode's synchronization location. In the unsteady simulations of the roughness configurations, a blowing-suction actuator introduces an upstream broadband Gaussian pulse. Fourier decomposition of the pulse's history shows that the single roughness strip attenuates frequencies higher than 208 kHz while lower frequencies are amplified. Likewise, the roughness array exhibits similar results, attenuating frequencies higher than 164 kHz and amplifying lower frequencies downstream. The results show that both configurations can delay second mode instability growth on a hypersonic blunt cone and possibly delay turbulent transition. However, investigations of the roughness effect's behavior downstream of the roughness configurations show that disturbance growth resumes and becomes more destabilizing to the boundary layer.

I. INTRODUCTION

Boundary layer transition from laminar to turbulent flow is a well-known problem for hypersonic vehicles and must be considered when designing such vehicles.[1] When a hypersonic boundary layer becomes turbulent, skin friction on the vehicle increases significantly. The increased skin friction, in turn, has a first-order impact on surface heating.[2] Due to its high speed, the surface heating imparted to the vehicle's airframe necessitates using a thermal protection system (TPS). TPS, such as ablative shielding or ceramic tile, typically adds significant weight to the airframe and, in turn, limits the range and payload of hypersonic vehicles.

In order to mitigate the adverse effects of surface heating, a way to control the boundary layer and maintain laminar flow is desired. Laminar–turbulent transition is the nonlinear response of a laminar boundary layer to various environmental disturbances.[3] There are several transition pathways to turbulence, but of primary concern to this paper is transition in low-disturbance environments.[4] The pathway involves receptivity of environmental noise, linear eigenmode growth, and nonlinear breakdown to turbulence. In hypersonic flows, Mack's second mode instability is responsible for the eigenmode growth and eventual destabilization of the boundary layer. Hence, control of the boundary layer and maintenance of a laminar flow can be obtained by attenuating this instability.

Surface roughness is one such source of environmental noise and has been studied extensively in laminar–turbulent transition research.[5,6] The main motivation behind roughness research is severalfold: first, to study turbulence by tripping laminar flow, to determine whether roughness will cause early transition, and, relatedly, to determine an upper bound where wall roughness (i.e., surface finish) will not affect natural transition.[5] From these motivations, research has

found that roughness can promote the laminar–turbulent transition in three different ways, which are the production of wakes with unstable shear layers, streamwise vorticity, and interaction with freestream disturbances.[5] The perturbations introduced to the boundary layer by the roughness then grow through various instability mechanisms, such as stationary crossflow, Görtler instability, transient growth, and Mack's second mode.[5] Currently, a general theory for roughness-induced transition has yet to be developed, but it has produced several valuable models, such as a criterion for transient modal growth on slender cones.[7] It has also motivated reexaminations of classic problems, such as the transition-reversal phenomenon and its sensitivity to surface finish.[8] However, recent research has shown that surface roughness can do more than promote laminar–turbulent transition and may provide a means to delay transition.[9,10]

Research into discrete surface roughness has shown that it can attenuate specific frequency ranges of the second mode instability and is a suitable approach to controlling the boundary layer.[9,10] These unique instances where roughness counter-intuitively attenuates the second mode instability are caused by the so-called "roughness effect" phenomenon. The roughness effect, illustrated in Fig. 1, occurs when discrete roughness elements shorter than the boundary layer thickness are placed at the synchronization location for a desired cutoff frequency of the second mode instability. The result is the attenuation of second mode frequencies higher than the cutoff frequency and the amplification of lower frequencies. By applying a series of discrete roughness elements further downstream, the previously amplified lower frequencies are attenuated, and in this way, Mack's second mode instability can be attenuated indefinitely. Thus, the roughness effect can be used to delay transition in low-noise environments. The roughness effect was first studied extensively by Duan *et al.*[9] and Fong *et al.*[10]

In 2010, Duan *et al.* began studying how discrete roughness could be used to stabilize hypersonic boundary layers.[9] The computational study looked at the effect different discrete roughness locations had on a single frequency pressure pulse on a two-dimensional (2D) flat plate in a Mach 5.92 flow. The study found that the pressure perturbation was attenuated when the roughness element was located downstream of the frequency's synchronization location—the point where the phase speeds of the discrete modes F and S intersect. In contrast, the pressure perturbation was amplified when the roughness element was upstream of the frequency's synchronization location.

Following up on the synchronization location insight, Fong *et al.* engaged in an extensive study of the roughness effect. One of Fong *et al.*'s first numerical studies investigated the effect of roughness location and heights as a function of local boundary-layer thickness. The pressure perturbations were attenuated for roughness placed at the synchronization location and farther downstream, with the tallest roughness resulting in the most robust attenuation.[11] With the importance of the synchronization location firmly established for a single frequency, Fong *et al.* proceeded to investigate the response of broadband disturbances to single roughness elements.[10] By introducing a low amplitude Gaussian pulse with a continuous frequency spectrum, Fourier decomposition was used to decompose the perturbation and study the evolution of different perturbation frequencies. The decomposition showed that frequencies lower than the roughness's synchronization frequency were amplified and remained amplified downstream, while frequencies higher than the synchronization frequency were strongly attenuated downstream. In this study, Fong *et al.* also considered using multiple roughnesses for the first time. By implementing a second downstream roughness element, frequencies previously amplified by the first roughness were attenuated by the second roughness. Moreover, frequencies attenuated by the first roughness were attenuated further. With these results, Fong *et al.* hypothesized that successive roughness elements could persistently attenuate unstable frequencies and be used to control boundary layer transition passively.

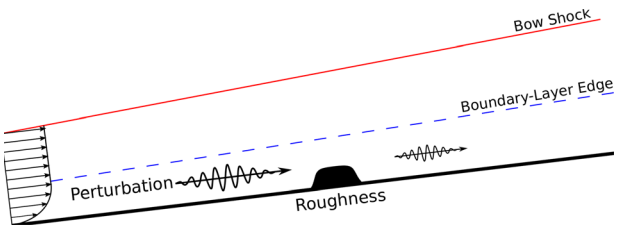

FIG. 1. Illustration of the roughness effect where a discrete roughness element is placed within the boundary layer to attenuate Mack's second mode instability.

The research of Duan and Zhong and Fong *et al.* led to the development of a patented passive laminar flow control method,[12] which uses the linear stability theory and N-factor analysis to position and dimensionalize roughness elements to attenuate boundary layer instabilities.

Prior to investigations by Duan and Zhong and Fong *et al.*, there were several instances of experiments encountering the transition-delaying phenomenon published in the literature. The first was by James in 1959, who noted that for a given Mach number, an optimum roughness height would produce a maximum laminar run.[13] Holloway and Sterret found in 1964, when studying Mach 4 and 6 flows, that under certain circumstances, roughness with a height less than the boundary layer thickness can delay transition.[14] More recently, Fujii experimentally found that 2D wavy wall roughness can delay transition.[15] Chynoweth *et al.* studied three-dimensional (3D) isolated roughness in which certain heights interacted with Mack's second mode instability without tripping the boundary layer.[16] In these previous investigations, the delayed transition was noted but not extensively investigated.

Following Fong's extensive numerical investigation on the roughness effect, the work was corroborated in an experimental validation with Prof. Schneider's group at Purdue University on the proposed boundary layer control method.[17] The experiment showed a reduction in the laminar breakdown and appeared to validate the transition-delaying roughness design on a compression cone. However, of interest to the present investigation, no unsteady simulation of the roughness configuration was carried out prior to the experiment, limiting our ability to probe the synchronization location criterion central to the passive boundary layer control strategy. Moreover, the experiment was performed on a compression cone with a nearly constant boundary layer thickness, limiting the experiment to one unstable frequency. This contrasts with the straight cones utilized in this paper, where boundary layer growth causes a range of second mode frequencies.

Around the same time, Tang *et al.* performed an experimental investigation of the second mode instability on a flat plate with 2D roughness.[18] The roughness was placed upstream of the synchronization point between modes F and S. They found that the second mode instability is amplified upstream of the roughness, attenuated

downstream, and resumes growth farther downstream. The experimental results confirmed Fong *et al.*'s numerical findings. Tang *et al.* also observed that the roughness height directly affects the amplification and damping of the instability.

Mortensen and Zhong simulated a real-gas flow over a flat plate with a 2D roughness element.[19] The results showed that the roughness effect extends to real-gas flow. Moreover, the study found that a real-gas flow is more effective at stabilizing the second mode instability in high Mach number and high enthalpy flows, where perfect-gas assumptions are invalid.

Sescu *et al.* investigated the response of boundary-layer disturbances to various two-dimensional surface nonuniformities.[20] These nonuniformities included a forward step, a backward step, a forward–backward step combination, a backward–forward step combination, a surface hump, a surface dip, and sinusoidal walls above and below the mean surface. They found that all surface feature configurations could reduce the amplitude of boundary layer disturbances to a certain degree, based on their shape and localized behavior, except for the dip and backward–forward step combination. A significant insight from this study is that surface features with adverse pressure gradients followed by favorable pressure gradients are more likely to reduce the amplitude of disturbances propagating inside the boundary layer.

More recently, Dong *et al.* developed an asymptotic theory that incorporated mean-flow distortions due to surface roughness to study its effect on the receptivity of discrete boundary layer modes.[21] This theory was extended and utilized by Dong and Zhao[22] to study the role of roughness in stabilizing or destabilizing the boundary layer near the synchronization location. They found that their theory agrees with Fong *et al.*'s[10,17] results and provide descriptions of two opposing factors: (1) the interaction between the mean-flow distortion and oncoming Mack mode and (2) inhomogeneous forcing from the curved wall, whose competition leads to scattering of the oncoming mode. Dong and Zhao also investigate the effect of roughness proportions and surface indentations.

Finally, in the space of using surface roughness as a passive control strategy, roughness has recently been investigated for its ability to control crossflow vortex positions. Berridge *et al.* placed spanwise arrays of roughness elements near the neutral point of the HIFiRE-5 geometry in an attempt to create counter-rotating vortexes that would weaken the crossflow instability.[23] Their experimental investigation showed some potential to control the strength of crossflow instabilities. However, it should be noted that their approach to delaying transition is different from the roughness effect phenomenon approach detailed in this paper.

To date, there has been substantial quality research on the roughness effect phenomenon, but each with its limitations. Experimentally, Fujii studied surface roughness on a cone and saw a delay in laminar–turbulent transition. However, the study did not consider the synchronization location in its placement of the roughness, nor did it focus on the roughness's immersion within the boundary layer. The Purdue experiment, while utilizing the linear stability theory (LST) to design and place the roughness elements and providing experimental evidence of delayed transition, was performed on a flared cone, limiting the experiment to nominally constant boundary layer thickness and a single unstable frequency. The single unstable frequency leaves the ability of the roughness effect to attenuate a range of frequencies higher than the cutoff frequency untested. Moreover, the ability of a roughness array to attenuate the second mode instability over its entire unstable frequency range is left unexamined. Computationally, Duan and Fong's extensive studies provide much of the groundwork to develop a passive boundary layer control method. However, their studies are limited to the direct numerical simulation (DNS) of 2D flat plates and do not consider more realistic hypersonic flow fields. Most of their studies are also limited to the same Mach 5.92 flow field, leaving most of the conditions where the roughness effect might exist unexplored.

There is still much to learn about the roughness effect phenomenon. For instance, it is not clear from the past research if the roughness effect extends to the conical flow fields of straight blunt cones with growing boundary layers. Many practical hypersonic applications have conical flow fields, and the effects of bluntness and surface roughness in those flow fields are an area of active research.[8,24–26] However, there is a lack of research on the roughness effect phenomenon in this area. Also missing is a complete computational and experimental investigation of the phenomenon where DNS results are rigorously compared with experimental results. Furthermore, the far downstream behavior of the roughness effect needs investigating. It is unknown whether the roughness effect actually stabilizes the second mode instability or momentarily attenuates its amplitude. Finally, a more comprehensive range of Reynolds number and Mach number flows needs investigation, as well as off-design flow conditions, such as variations in Mach number or angle-of-attack.

This paper will investigate two roughness configurations: one of a single axisymmetric roughness and another of an array of six axisymmetric roughness. The purpose of the first configuration is to research the effect of a single roughness element in a conical flow and investigate its long-term downstream effects. The second configuration is to research how effectively an array stabilizes the boundary layer.

The paper is organized as follows: the governing equations and computational methodology are introduced in Sec. II and followed by the investigation's results in Sec. III. This section is divided into several parts with the LST analysis in Sec. III A, the design of the transition-delaying roughness configurations in Sec. III B, the unsteady simulation results in Sec. III C, and the Fourier decomposition results in Sec. III D. A brief description of the Passive Laminar Boundary Layer Control Method strategy is provided alongside the design in Sec. III B. The final discussion and conclusion are given in Sec. IV.

II. GOVERNING EQUATIONS AND COMPUTATIONAL METHODOLOGY

This paper uses direct numerical simulation of the three-dimensional Navier–Stokes equations to obtain steady and unsteady hypersonic flow solutions over a blunt cone. The DNS code utilizes a unique approach of high-order accurate schemes and shock-fitting to accurately compute the bow shock's location and movement over conical geometries.[27] Surface roughness in the form of a single circumferential strip or an array of circumferential strips is implemented by mapping an analytical shape onto the frustum of the cone. The mapping makes it possible to apply a body-fitted grid over the roughness strips and maintain a high-order accurate solution around them. Numerical simulations are obtained by first converging a steady-state flow solution, followed by an unsteady simulation using a blowing-suction actuator. The actuator is placed upstream of the roughness elements and releases a Gaussian pulse. Stability analysis is conducted

with linear stability theory on steady-state flow solutions and Fourier decomposition on unsteady simulations.

A. Governing equations

The DNS code solves the conservation-law form of the three-dimensional Navier–Stokes equations in Cartesian coordinates. Written in vector form, the governing equations are

$$\frac{\partial \boldsymbol{U}}{\partial t}+\frac{\partial \boldsymbol{F}_j}{\partial x_j}=\frac{\partial \boldsymbol{G}_j}{\partial x_j}, \tag{1}$$

where $\boldsymbol{U}$ is the state vector of conserved quantities, $\boldsymbol{F}_j$ is the inviscid flux vectors, and $\boldsymbol{G}_j$ is the viscous flux vector in the jth spatial direction. The state and flux vectors are defined as

$$\boldsymbol{U}=\{\rho,\rho u_1,\rho u_2,\rho u_3,e\}^T, \tag{2}$$

$$\boldsymbol{F}_j=\{\rho u_j,\rho u_1u_j+p\delta_{1j},\rho u_2u_j+p\delta_{2j},\rho u_3u_j+p\delta_{3j},(e+p)u_j\}^T \tag{3}$$

and

$$\boldsymbol{G}_j=\{0,\tau_{1j},\tau_{2j},\tau_{3j},\tau_{jk}u_k-q_j\}^T, \tag{4}$$

where e is the internal energy, τ_{ij} is the viscous stress tensor, q_j is the heat flux, and δ is the Kronecker delta. The internal energy, viscous stress, and heat flux are defined as follows:

$$e=\rho\left(c_vT+\frac{1}{2}u_ku_k\right), \tag{5}$$

$$\tau_{ij}=\mu\left(\frac{\partial u_i}{\partial x_j}+\frac{\partial u_j}{\partial x_i}\right)-\frac{2}{3}\mu\frac{\partial u_k}{\partial x_k}\delta_{ij}, \tag{6}$$

$$q_j=-\kappa\frac{\partial T}{\partial x_j}. \tag{7}$$

For the low freestream enthalpy simulation under consideration, Eq. (1) is closed, assuming a calorically perfect gas

$$p=\rho RT, \tag{8}$$

where R is the specific gas constant of nitrogen gas. Nitrogen gas is used in Sandia National Laboratory's (SNL) Hypersonic Wind Tunnel (HWT-8) facilities and is consistent with the experimental conditions from which the present simulation takes its parameters.[28] The specific heats, c_p and c_v, are held constant with a given specific heats ratio of $\gamma=1.4$. The viscosity coefficient, μ, is calculated using Sutherland's law[29] in the following form:

$$\mu=\mu_r\left(\frac{T}{T_o}\right)^{3/2}\frac{T_o+T_s}{T+T_s}, \tag{9}$$

where $\mu_r=1.7894\times10^{-5}$ N s/m^2, $T_o=288.0$ K, and $T_s=110.33$ K. Finally, the thermal conductivity, κ, is computed by

$$\kappa=\frac{c_p\mu}{Pr} \tag{10}$$

with a constant Prandtl number of 0.72. This formulation of the governing equations has been used previously by Fong *et al.*,[10] Huang and Zhong,[30] and Lei and Zhong[31] to simulate perfect gas hypersonic flow.

B. Shock-fitting and numerical approach

Shock-fitting is used to obtain an accurate bow shock location over the blunt cone's nose and body. The shock-fitting method treats the bow shock as the upper boundary of the physical domain by computing the location of the bow shock produced by the blunt cone. Equation (1) is solved in a computational domain with body-fitted curvilinear coordinates (ξ, η, ζ, τ), where ξ is in the direction of the cone surface, η is normal to the cone surface, ζ is in the circumferential direction, and τ is the time. Full transformation details between the computational space and physical space can be found in Ref. 27.

By treating the shock as a domain boundary, the shock's location and transient movement are solved with an additional ordinary differential equation alongside the governing equations. This is accomplished by taking the Rankine–Hugoniot relations, which provide the flow boundary conditions across the shock, as a function of the front shock velocity v_n, and a characteristic compatibility equation for v_n behind the shock. The resulting ordinary differential equation is solved for a static shock position. A complete derivation shock-fitting equation can also be found in Ref. 27.

An explicit fifth-order upwind scheme and an explicit sixth-order central finite-difference scheme are used to discretize the inviscid and viscous terms of Eq. (1) in the ξ and η-directions. Second derivatives are obtained by applying the schemes twice. Derivatives in the ζ-direction are computed using Fourier collocation. Finally, fifth-order Lax–Friedrichs flux splitting is applied to the inviscid flux terms, and a low storage third-order Runge Kutta method[32] is used to converge the steady-state and advance the unsteady solutions.

C. Freestream and simulation conditions

The simulation in this paper is of a straight blunt cone at zero angle-of-attack. The cone has a 7° half-angle and a nose radius of 0.5 mm with a total length of 1.10 m measured from the blunt nose tip. The simulation is axisymmetric. Freestream conditions are taken from a previous experiment[28] performed in SNL's HWT-8 facilities for the same blunt cone geometry with a length of 0.534 m. The freestream conditions and simulation parameters are tabulated in Table I.

D. Discrete body-fitted roughness

This paper examines two-surface roughness configurations. The first is a circumferential strip designed to study a single strip's effect on the attenuation of boundary layer instabilities. The second configuration is an array of six sequential circumferential roughness strips designed to study the continued attenuation of boundary layer instabilities. The discrete surface roughness in this paper is achieved by mapping the function of an analytical shape to the cone's frustum.

TABLE I. Simulation parameters.

Parameter	Value	Parameter	Value
M_∞	8.0	T_w/T_∞	6.21
ρ_∞	0.024 803 kg/m^3	T_w/T_{ad}	0.52
p_∞	330.743 Pa	T_w	279.0 K
$h_{0,\infty}$	0.597 MJ/kg	Re_∞/l	9 584 257 m^{-1}
U_∞	1093.07 m/s		

The body-fitted grid transformation, necessitated by the shock-fitting approach, requires that the analytical shape have continuous derivatives throughout the domain. Consequently, this limits us to shapes with smooth-edged cross-sections and excludes sharp-edged geometries. However, by limiting the roughness to smooth shapes, the high-order accuracy of the solution is preserved.

Past research on the roughness effect has investigated the importance of a roughness element's overall height, width, and spacing, with some attention paid to the physical geometry (e.g., elliptical strip vs square strips).[20,33] Experiments and simulations with comparable results but different cross-sectional geometries have shown that roughness shape has minimal influence on the attenuation of the boundary layer instabilities when compared to its overall height. The cross-sectional geometry in this investigation was chosen to closely approximate the layered thermal tape used in Ref. 17.

The single roughness shape is defined by the difference of two hyperbolic tangents

$$y'(x',z') = \frac{1}{2}h\left\{\tanh\left[q\left(x'+\frac{w}{2}\right)\right] - \tanh\left[q\left(x'-\frac{w}{2}\right)\right]\right\}, \quad (11)$$

where x', y', and z' are the Cartesian coordinates prior to being mapped to the cone surface. The parameters h and w control the height and width of the roughness, and q is a free parameter that controls the edge smoothness. Similarly, the roughness array is defined as the summation of multiple elements

$$y'(x',z') = \frac{1}{2}\sum_{i=1}^{N} h_i\left\{\tanh\left[q\left((x'-l_i)+\frac{w_i}{2}\right)\right] - \tanh\left[q\left((x'-l_i)-\frac{w_i}{2}\right)\right]\right\}, \quad (12)$$

where N is the number of elements, and l_i is the distance of element i to the first element in the array. Equations (11) and (12) are mapped to the cone's frustum using the following rotation and translation equations:

$$\begin{aligned} x &= \cos\left(\theta_{\frac{1}{2}}\right)x' - \sin\left(\theta_{\frac{1}{2}}\right)y' + x_c, \\ y &= \left[\sin\left(\theta_{\frac{1}{2}}\right)x' + \cos\left(\theta_{\frac{1}{2}}\right)y' + y_c\right]\cos(\theta), \\ z &= \left[\sin\left(\theta_{\frac{1}{2}}\right)x' + \cos\left(\theta_{\frac{1}{2}}\right)y' + y_c\right]\sin(\theta), \end{aligned} \quad (13)$$

in which x, y, and z are the Cartesian coordinates in the physical domain, $\theta_{\frac{1}{2}}$ is the cone half-angle, θ is the angle in the azimuthal direction about the cone, and x_c and y_c are the surface location of the roughness center at $\theta = 0$. Applying Eq. (13) to Eq. (11) produces a circumferential roughness strip on a cone similar to the experimental configuration used in Ref. 17.

E. Linear stability analysis of steady-state

In this investigation, the stability characteristics of the boundary layer are studied using the linear stability theory (LST). LST uses the boundary layers profiles from the steady-state solution to provide the modal phase speeds, growth rates, neutral points, and mode shapes results over a wide range of frequencies. More specifically, LST analysis in the hypersonic regime solves for the eigenvalue and eigenfunctions of the Fast and Slow discrete modes (modes F and S), which are responsible for Mack's second mode instability found in hypersonic boundary layers.[34]

The analysis is conducted with a compressible LST code originally developed by Ma and Zhong[35,36] following the work done by Malik.[37] The compressible LST equations are obtained from an instantaneous solution, comprised of a steady term and a fluctuating term, substituted into the compressible Navier–Stokes equations and expanded. The collection of steady terms which satisfy the governing equations are removed from the expansion. The remaining steady terms, which form products with the fluctuating terms, are obtained from the steady-state solution and assumed to be locally parallel becoming a function of the wall-normal direction, y, only. Higher-order fluctuating terms are assumed to be small and are linearized. Finally, a normal mode solution is assumed for the fluctuations of the following form:

$$q'(x,y,z,t) = \hat{q}(y)\exp\left[i(\alpha x + \beta z - \omega t)\right], \quad (14)$$

where q' is the vector of fluctuating variables $\{u', v', p', T', w'\}^T$, $\hat{q}$ is the vector of their complex eigenfunctions, (x, y, z) describe the wall coordinate frame, α and β are wavenumbers in the x and z-direction, and ω is the circular frequency. Applying a 2D spatial amplification theory approach to Eq. (14), α is taken as complex, β is zero, and ω is a real number. Substituting in the normal mode solution for the fluctuating terms results in a coupled set of five ordinary differential equations

$$\left(\mathbf{A}\frac{d^2}{dy^2} + \mathbf{B}\frac{d}{dy} + \mathbf{C}\right)\hat{q}(y) = 0, \quad (15)$$

where **A**, **B**, and **C** are the complex square matrices found in Ref. 37. Equation (15) constitutes an eigenvalue problem wherein Dirichlet boundary conditions are applied at the surface and far-field. Malik's multi-domain spectral method approach and a packaged complex eigenvalue solver are used to solve the resulting eigenvalue problem. Solving Eq. (15) for complex α provides the solution to the dispersion relation, $\alpha = \Omega(\omega)$, and the complex eigenfunction vector, $\hat{q}$.

F. Simulation of an unsteady disturbance with surface roughness

Unsteady simulations are computed from the Navier–Stokes equations by introducing an unsteady disturbance into a steady-state base flow and advancing the simulation. The steady-state base flow comes from the previously converged steady-state solution used in the LST analysis. The unsteady disturbance originates from a blowing-suction actuator that extends circumferentially around the cone and is placed upstream of the roughness locations. The circumferential actuator slot ensures the unsteady simulation remains axisymmetric. The actuator introduces an unsteady mass flux into the steady-state base flow. The flux is sinusoidal in space and has a Gaussian amplitude in time. The pulse's sinusoidal period prevents additional mass from entering the simulation, while the Gaussian amplitude introduces a broad frequency spectrum that includes the most unstable mode frequencies for the flow conditions.

The blowing-suction actuator's mass flux per unit area follows the equation

$$\dot{m}_p(s,t) = \varepsilon(\rho U)_\infty \exp\left(\frac{-(t-\mu)^2}{2\sigma^2}\right)\sin\left(2\pi\frac{s-s_c}{l}\right), \quad (16)$$

for $s_c < s < s_c + l$ and $t > 0$, where s is the surface location measured from the nose tip, s_c is the actuator's surface location, l is the length of the actuators opening, μ is the mean of the Gaussian pulse, and σ is its standard deviation. The mass flux is scaled by $\varepsilon(\rho U)_\infty$, where imposing a small ε keeps the flowfield's response linear and prevents nonlinear interaction between frequencies. In this way, the disturbance created by the pulse can be decomposed, and each frequency studied independently. The mean of the pulse, μ, is defined in terms of a minimum mass flux, $(\rho v)_{\min}$, the initial mass flux at $t = 0$, where

$$\mu = \sqrt{-2\sigma^2 ln\left(\frac{(\rho v)_{\min}}{\varepsilon(\rho U)_\infty}\right)}. \quad (17)$$

By defining μ in this way, it can be fixed with a reasonable $(\rho v)_{\min}$ regardless of the simulation conditions. The only remaining free parameter in Eq. (16) is the standard deviation, σ, which permits direct control over the pulse's frequency content. The standard deviation in Table II produces a pulse with a nominal spectrum greater than 1 MHz, which is sufficient for the range of unstable mode frequencies found in the unsteady simulation. Table II contains the remaining pulse parameters used in this paper. The technique of using a Gaussian pulse to examine mode amplification/attenuation was previously implemented by Fong *et al.*[11] and Knisely and Zhong.[38,39]

Conducting an unsteady simulation involves initiating the pulse, allowing it to propagate along the cone surface and exit at the downstream domain boundary. The time history of the surface pressure (along with other state variables) is recorded along the cone surface. This temporal surface pressure data are decomposed into a frequency spectrum using Fourier analysis in order to analyze the growth, decay, and attenuation of individual frequencies. The resulting spectrum is also normalized by the spectrum of the initial Gaussian pulse in order to compare frequencies of different initial amplitudes.

III. RESULTS AND DISCUSSION

The DNS simulation begins by computing the smooth cone steady-state solution from the freestream parameters described in Table I. From this solution, linear stability analysis is performed to determine the stability characteristics of the boundary layer. These stability results, in turn, guide the design of the transition-delaying roughness strips. As mentioned previously, two roughness configurations are examined: a single strip and an array of six strips. These configurations are then applied to the cone surface, and the steady-state solutions with roughness are re-computed. With the converged solutions, unsteady simulations are computed using a blowing-suction actuator. A Fourier decomposition of the unsteady results is performed, and the cases are compared.

TABLE II. Gaussian pulse parameters for DNS.

Parameter	ε	$(\rho v)_{\min}$ (kg m/s)	σ (μs)	μ (μs)	s_c (m)	l (mm)
Value	10^{-3}	10^{-10}	0.3	2.0398	0.1	1.9703

A. Stability results of steady-state by LST

With the steady-state solutions in hand, a preliminary spatial stability analysis of the steady-state at an arbitrary frequency is conducted to determine which of the discrete boundary layer modes, F or S, is responsible for Mack's second modal instability. After identifying mode S as the unstable mode, a neutral stability curve for the mode is computed over the cone's surface. The curve, provided in Fig. 2, contains all the points where the growth rate of mode S is zero. The neutral stability curve itself is composed of two branches: branch I and branch II. Branch I demarks the point where mode S, at an arbitrary frequency, will destabilize when propagating downstream—conversely, branch II indicates the point where the mode re-stabilizes. More importantly, the two branches enclose an area of unstable growth rates, while the area outside of the branches contains stable growth rates. Figure 2 also contains a dashed line demarking a segment of the synchronization curve for modes F and S from 150 to 500 kHz. The synchronization curve will be discussed later in this subsection.

Figure 2 shows that the mode S unstable frequency range extends from 101 to 647 kHz, as seen along branch I. Likewise, frequencies between 139 and 647 kHz are able to re-stabilize before the end of the cone, as seen along branch II. Moreover, the figure illustrates how lower frequencies are more likely to lead to transition due to the unstable region's curved shape. At lower frequencies, the branches are farther apart, giving even moderate growth rates ample distance over which to grow.

With the unstable frequency range known, it is possible to compute the N-factor values of mode S. The N-factor comes from the e^N method of transition prediction, which attempts to correlate values of N with experimentally obtained transition locations.[40,41] The N-factor calculation quantifies how unstable a frequency becomes by integrating its modal growth rate, α_i, over its unstable region. The N-factor is defined as

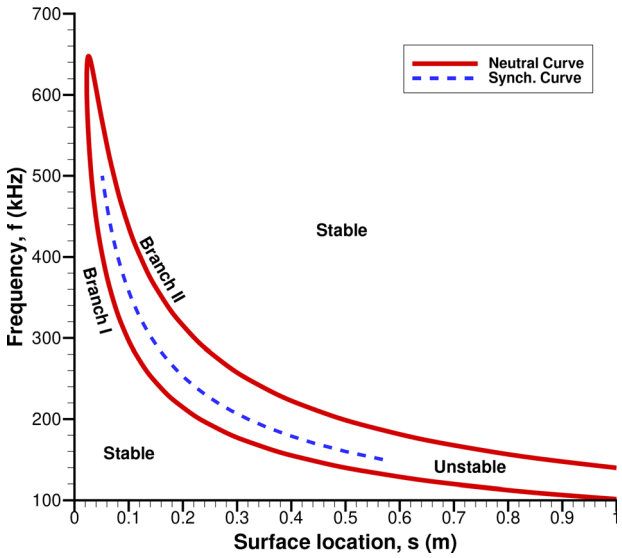

FIG. 2. Neutral curve for mode S exhibiting Mack's second mode instability.

$$N(\omega, s) = \int_{s_o}^{s} -\alpha_i ds, \tag{18}$$

where s is the distance along the surface, s_o is the location of the branch I neutral point as seen in Fig. 2, ω is the frequency, and α_i is the growth rate. The growth rate is found using LST and the steady-state boundary layer profiles.

The N-factor values for Mack's second mode instability over a range of frequencies are plotted in Fig. 3. The figure plots frequencies between 140 and 420 kHz in 20 kHz increments, with the frequencies of 140, 280, and 420 kHz highlighted as reference datums. The selected frequency range provides the most relevant N-factor coverage over the cone. As expected, the unsteady frequencies decrease downstream with higher frequencies on the left and lower frequencies on the right. The range of N values nominally starts from zero at 35 mm from the nose tip and peaks at a maximum value of 10.6 at the end of the cone. The maximum value of N at any particular point on the cone can be determined from the blue-lined envelope traced out by the frequency curves.

The steady increase in N's value downstream is consistent with the neutral stability curve in Fig. 2, where a sufficiently wider unstable region at lower frequencies can produce large N values with moderate growth rates. For this reason, it is important to be aware of the lower unstable frequencies and devise a passive boundary layer control strategy to attenuate them.

As a transition prediction method, the e^N method correlates N values with transition location. For the purposes of designing a transition-delaying roughness element, the e^N method is used to determine the frequency of the dominant instability at the transition location. In the experiment from which this paper takes its simulation parameters, Casper *et al.* found that instability wave intermittency begins to decrease, and intermittent turbulence starts to increase at

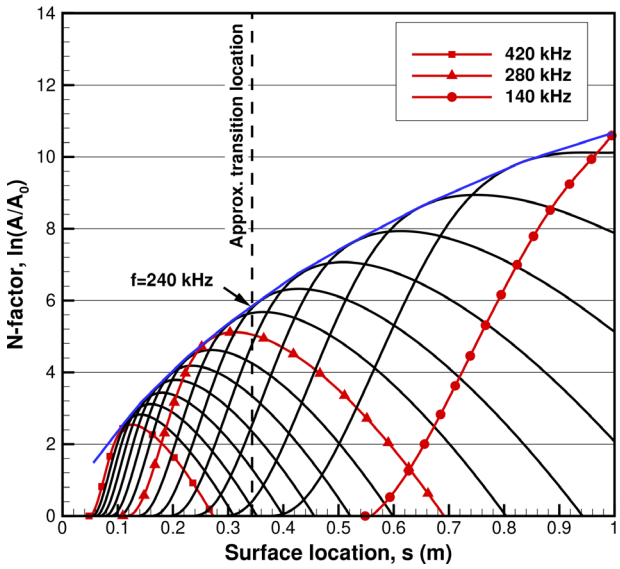

FIG. 3. Mode S N-factor for Mack's second mode instability. Frequencies range from 140 to 420 kHz in increments of $\Delta f = 20$ kHz. The blue curve traces the local value of N.

0.340 m along the cone surface.[28] Using 0.340 m as the estimated point of transition, Fig. 3 shows that the largest N value at this location is approximately 5.7 for a frequency of 240 kHz. Taking 240 kHz as the mode S frequency most likely to start turbulent transition, the frequency is targetted and attenuated using surface roughness.

With a target frequency identified, the next step in the design process is determining its synchronization location. The synchronization location is where the phase speed of modes F and S intersect in a spatial stability analysis. Figure 2 shows the point of intersection as the synchronization curve. Notice that the synchronization location is a function of frequency and lies between the branches of the neutral stability curve. The research conducted by Fong *et al.* conclusively found that identifying the frequency that produced a synchronization between modes F and S at the location of a roughness element ultimately determines which range of second mode instability frequencies will be amplified and which will be attenuated.[10,11,17,33,42] The synchronization location is essential to making the transition-delaying roughness control strategy work. However, Fong *et al.*'s work is limited to flat plate planar flows, and it is unclear if the synchronization location criterion is applicable in conical flow, which is a primary motivation of this investigation.

The intersecting phase speeds used to identify the synchronization location are the result of weak coupling between modes F and S.[43] This weak coupling is important to note because it not only synchronizes the phase speeds but also gives rise to Mack's second mode instability through a process of intermodal exchange. The phase speed plot in Fig. 4(a) shows that for a frequency of 240 kHz, modes F and S synchronize at $s = 0.2223$ m. According to Zhong *et al.*'s passive hypersonic boundary-layer control strategy, placing a properly sized roughness element at this location will attenuate unstable frequencies lower than 240 kHz (Ref. 12). In some instances, a clearly defined synchronization location is difficult to obtain. However, in this instance, there is no ambiguity in the intersection of modes F and S, indicating this case is well suited to investigate the roughness effect.

In addition to the phase speed, Fig. 4 contains the growth rates for modes F and S. Figure 4(b) shows that mode S is unstable for nearly a third of the cone's length: the second mode instability first appears at $s = 0.1570$ m and stabilizes at $s = 0.4880$ m. The figure also shows that mode F remains entirely stable, and no Tollmien–Schlichting instabilities (Mack's first modal instability) appear at the target frequency.

B. Roughness element design for delaying second mode growth

With the target frequency's synchronization location obtained from LST and boundary layer data available from the steady-state solution, the dimensions of the single circumferential roughness strip can be determined. A parametric study by Fong *et al.*[33] found that placing the roughness element at the synchronization location attenuated frequencies higher than the target frequency while amplifying lower frequencies. Thus, by placing the element slightly further downstream (i.e., at the synchronization location of a lower frequency), attenuation of the target frequency is guaranteed. The same parametric study investigated different configurations of roughness height and width, the most consistent attenuation coming from roughnesses that are half the local boundary layer thickness ($0.5\delta_{99}$) in height and twice the thickness ($2\delta_{99}$) in width. In a previous computational-experimental collaboration investigating transition-delaying roughness,[17] these same rules were used to

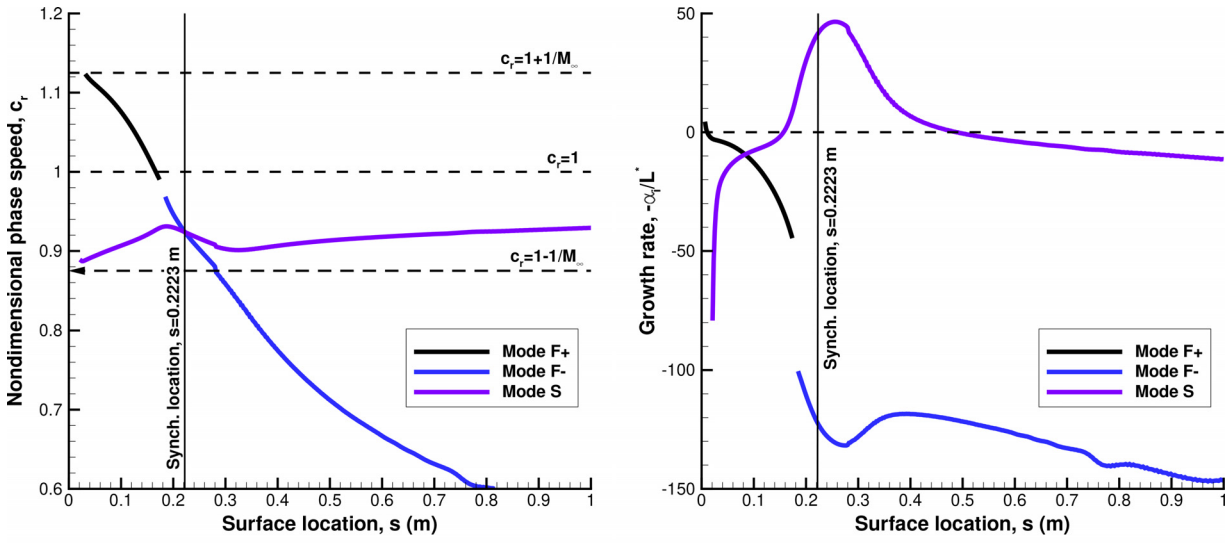

a) b)

FIG. 4. (a) Phase speed and (b) growth rate for mode F and S at 240 kHz. The vertical line in both graphs denotes the synchronization location at $s = 0.2223$ m.

design the roughness element and successfully attenuated Mack's second mode instability.

Following the convention set by Fong *et al.*[33] and used in Fong *et al.*[17] of placing the first roughness strip downstream of the target frequency, the roughness strip is placed 7.1 cm downstream of the target frequency's (240 kHz) synchronization location at $s = 0.2936$ m (a distance of approximately $44\delta_{99}$ downstream). The boundary layer thickness is measured using the δ_{99} criterion, where the velocity profile is equal to 99% of the freestream velocity. The roughness strips' height and width based on this thickness are listed in Table III.

Since the initial roughness strip's physical location is placed further downstream from the target frequency's synchronization location, it is prudent to identify the frequency that synchronizes at this location. The new roughness synchronization location was found by first non-dimensionalizing the phase speed results in Fig. 4(a) and then solving for $s = 0.2936$ m. This provides an approximate value for the frequency, which is refined using a bisection approach. As a result, the initial roughness strip location has a synchronization frequency of 208 kHz. Hence, the passive laminar flow control strategy predicts that the initial roughness strip will attenuate frequencies higher than 208 kHz while amplifying lower frequencies.

In order to attenuate Mack's second mode over a wider frequency range, multiple roughness strips are placed downstream of the first roughness. Following the procedure prescribed in Ref. 33 and used in Ref. 17, the downstream spacing of the strips is measured as 20 times the boundary layer thickness ($20\delta_{99}$) of the previous strip location. Since the boundary layer thickness increases downstream, the physical dimensions of each roughness strip also increase but with the same relative proportions to the local boundary layer mentioned above. The dimensions for the roughness array are listed in Table IV, the location of each strip is measured along the surface from the blunt nose tip.

Now that the single roughness strip and six strip array configurations have been designed, the steady-state simulations with roughness can proceed. The steady-state computation is an intermediate result needed to obtain a full unsteady roughness simulation. Due to non-parallel flow in the vicinity of the roughness strip, an LST analysis of the steady-state is not valid here and instead this paper relies on Fourier decomposition of the unsteady flow for analysis. Nevertheless, the rough steady-state does contain some notable features. For example, the streamwise pressure contours around the single roughness strip configuration in Fig. 5(a) show a Mach wave on the strip's upstream edge and an expansion fan on the downstream edge. The strip's presence significantly influences the upstream pressure field by

TABLE III. Roughness parameters of single roughness strip.

Parameter	Value	Unit
s	0.2936	m
δ_{99}	1.627	mm
h ($0.5\delta_{99}$)	0.8135	mm
w ($2\delta_{99}$)	3.254	mm

TABLE IV. Location and dimensions of each strip in the roughness array.

Strip	Surface location, s (m)	Nondim. location, s/r_n	Height, h (mm)	Width, w (mm)
1	0.2936	587.2	0.813	3.254
2	0.3261	652.2	0.864	3.457
3	0.3607	721.4	0.916	3.663
4	0.3973	794.6	0.955	3.819
5	0.4355	871.0	1.001	4.006
6	0.4756	951.2	1.053	4.211

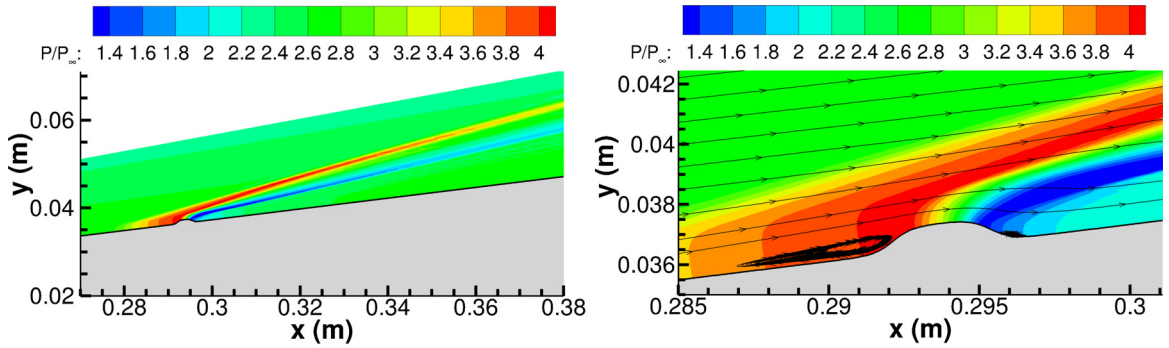

a) b)

FIG. 5. (a) Steady-state pressure contours around the single roughness strip configuration and (b) streamtraces denoting recirculation zones.

at least four widths, while the downstream pressure field shows considerably less influence. The unequal regions of influence are a notable departure from the flat plate simulations in Ref. 10, in which the strip's influence is "felt" nearly equally upstream and downstream. The cause for the decreased influence can be attributed to the lack of a downstream separation zone. As seen in the streamtrace plot in Fig. 5(b), the downstream separation zone is not only smaller than the flat plate case but is nearly non-existent compared to the extent of the upstream separation zone.

It is worth noting, however, that it is possible to perform a stability analysis in areas with non-parallel flow using a combination of the parabolized stability equations (PSE) and the harmonic linearized Navier–Stokes equations (HLNSE). PSE was previously used in Ref. 44 to study the roughness effect phenomenon, and a combination of PSE and HLNSE was used in Refs. 8, 25, and 26 to study discrete surface roughness and transient growth.

C. Unsteady results

This section presents the unsteady results for a no roughness comparison case, the single roughness strip case, and the roughness array configuration. The results include an axisymmetric view of the disturbance wave packet as it propagates downstream, the wave's surface pressure perturbation along a 1D ray of the cone's surface for the whole unsteady simulation, and instantaneous surface pressure perturbation traces at discrete time intervals. These results provide physical insight into the disturbance wave's downstream behavior, how it is affected by the roughness configurations, amplitude growth, and the long-term ability of the passive boundary layer control strategy to attenuate second mode instabilities. Later, these results will be decomposed with Fourier analysis to obtain the disturbance wave's frequency spectrum to show which second mode frequencies are attenuated.

1. Smooth surface cone

Using the steady-state simulation results as the base flow, a blowing-suction actuator is added to the smooth cone steady results at $s_c = 0.1$ m ($s/r_n = 200$), and the pulse defined by Eq. (16) and Table II is imposed on the flowfield. Figure 6 shows the instantaneous view of the normalized pressure perturbations after the pulse, which takes on the familiar "rope-like" shape of the second mode wave packet as it propagates downstream. In addition to the instantaneous view, the wave packet can be viewed for the whole unsteady simulation by its surface pressure perturbation along a 1D ray of the cone's surface (analogous to an $x - t$ diagram) in Fig. 7. The figure shows the wave packet's surface pressure perturbations as it propagates through the domain over time. The contour plot depicts the peaks and valleys of the wave packet as rays of constant speed originating from s_c. As the simulation progresses, the packet increases in width downstream due to wave dispersion within the boundary layer. This is because the many frequencies that comprise the wave packet travel at different wave speeds. The packet's wavefront has a constant speed of 1039 m/s ($0.95U_\infty$), which is below the freestream speed (U_∞) but above the slow acoustic speed of 956 m/s ($0.87U_\infty$), which is indicative of a wave packet comprised of mode S.

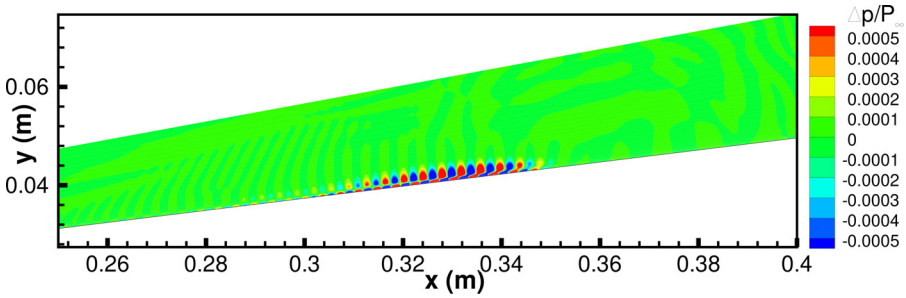

FIG. 6. Instantaneous normalized pressure perturbation contour, $\Delta p/P_\infty$, of the unsteady wave packet on a smooth cone.

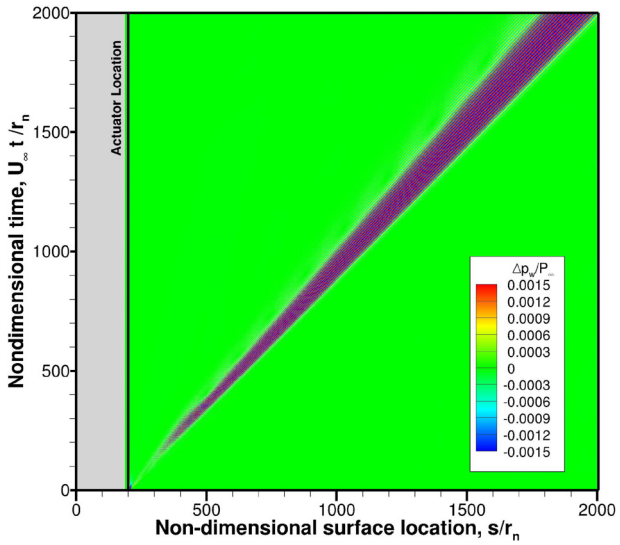

FIG. 7. The wave packet's surface pressure perturbation contours for all time on a smooth cone without roughness. Contour levels are clipped to emphasize the wave's structure and trajectories; max $|\Delta p_w/P_\infty| = 0.0094$.

For a closer look at the shape of the wave packet, the instantaneous surface pressure at five discrete time intervals are extracted from Fig. 7 and plotted in Fig. 8. The plots highlight the wave packets steady amplitude growth as it propagates downstream. Between the first and last subplots, the packet amplitude grows 1.48 times over a distance of $\Delta s/r_n = 1142$, indicative of an unstable growth rate and Mack's second mode instability. Later, in Sec. III D, these data will be decomposed with FFT to obtain the frequency spectrum of the wave packet and determine which frequencies are causing the amplitude growth. Finally, the packet's wavefront speed and amplitude growth are consistent with the mode S LST results in Fig. 4.

2. Single roughness strip configuration

Just as with the smooth cone steady-state, a blowing suction actuator is added to the single roughness strip cone steady-state, and a pulse is imposed on the flowfield. Figure 9 shows the wave packet as it propagates downstream toward the roughness element. Two instances of the packet are featured: when the packet is passing over the element [Fig. 9(a)], and when it is downstream of the element [Fig. 9(b)]. In Fig. 9(a), the packet is stretched and deformed as it passes over the element compared to the undistorted packet seen in Fig. 6. On close examination of the wave packet, the weaker pressure perturbation

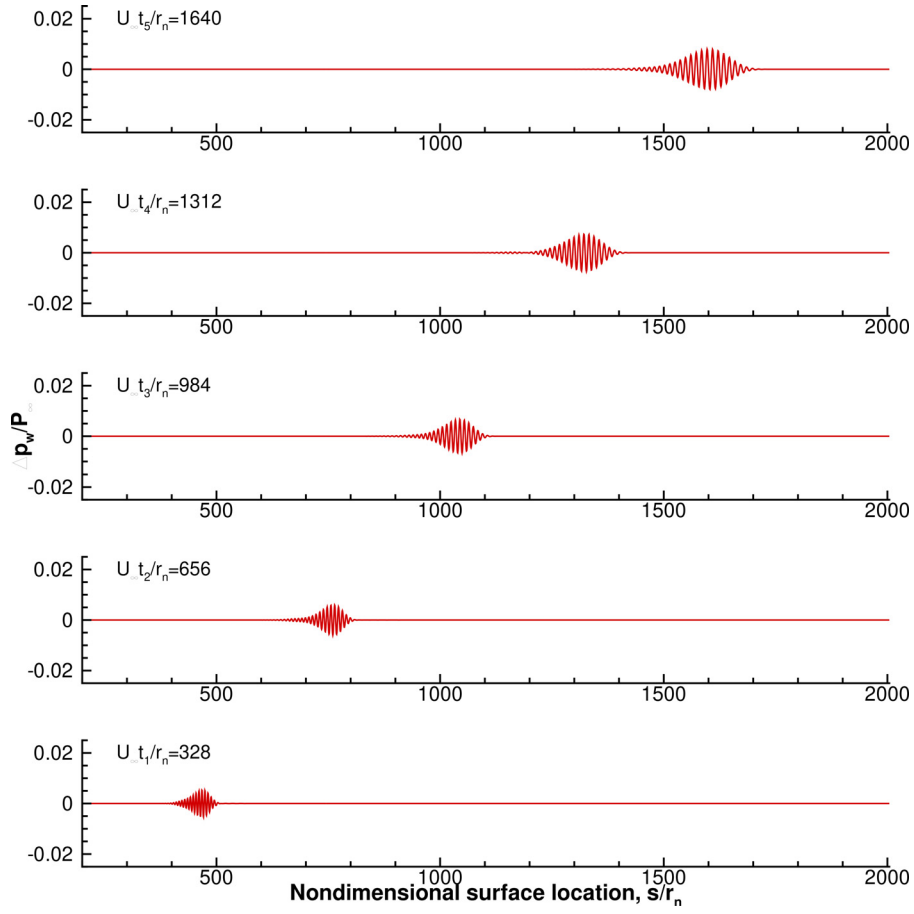

FIG. 8. Propagation of surface pressure wave along the cone surface with no roughness. The instantaneous pressure is plotted at five equal nondimensional time intervals of $U_\infty \Delta t/r_n = 328$ ($\Delta t = 0.15$ ms).

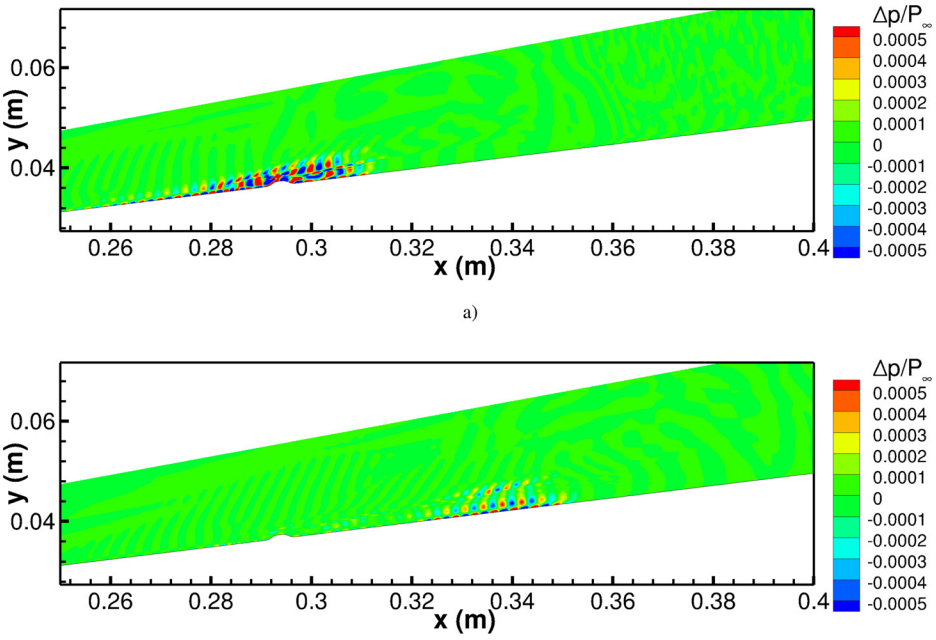

FIG. 9. (a) As the wave packet traverses the element, parts of it are pushed into flow behind the shock and "shed." (b) Significantly weakened wave packet downstream of the strip with dissipating perturbations. Contour levels are clipped to emphasize structures within the disturbance.

seen above the main perturbation appears to grow in amplitude as the packet negotiates the element's leading edge. These newly amplified perturbations attenuate quickly, disappearing just as they pass over the element. The strong off-the-wall perturbations seen in Fig. 9(b) are "shed" from the main wave packet as it passes down the trailing side of the element and propagates in the expansion fan. These shed features notwithstanding, the most significant feature of Fig. 9(b) is the attenuation of the perturbations on the wall.

The wave's surface pressure perturbation along the cone for the whole unsteady simulation is presented in Fig. 10. As designed, the single roughness strip is placed at the synchronization location, $s/r_n = 587.2$ ($s = 0.2936$ m), for the 208 kHz frequency intended to attenuate the 240 kHz frequency responsible for intermittent turbulence—the actuator is again located at $s/r_n = 200$ ($s_c = 0.1$ m). The contour plot makes it possible to view the wave packet as individual wave trajectories, with faster waves leading and slower waves following. The wavefront is visible throughout the unsteady simulation and does not change its angle of trajectory. This constant angle indicates that the roughness strip does not impede the wave packet's propagation speed. However, the trailing wave trajectories take on most of the amplitude attenuation. Overall, the single roughness strip attenuates the wave packet for a distance of $\Delta s/r_n = 200$–300 (0.1–0.15 m). As time progresses, these amplitudes begin to grow as anticipated, reaching a maximum disturbance pressure ratio of 0.0262.

Although Fig. 10 provides an entire overview of the wave packets propagation, it is difficult to discern the waves structure. Figure 11 features pressure perturbation traces along the surface taken at equal intervals of $U_\infty \Delta t/r_n = 328$ (0.15 ms) for the single roughness strip case. At $U_\infty t_1/r_n = 328$, the disturbance is upstream of the roughness strip and appears as a single wave packet. At $U_\infty \Delta t_2/r_n = 656$, the disturbance is just downstream of the roughness strip and is significantly reduced in amplitude as predicted by the roughness effect phenomenon. Advancing farther in time, the wave packet grows in amplitude from its attenuated state. This behavior is expected since mode S remains unstable. However, it is important to note that the packet's maximum amplitude grows 4.02 times between the initial plot and final plot, which is significantly higher than in the previous smooth cone case over the same distance. Finally, the disturbance

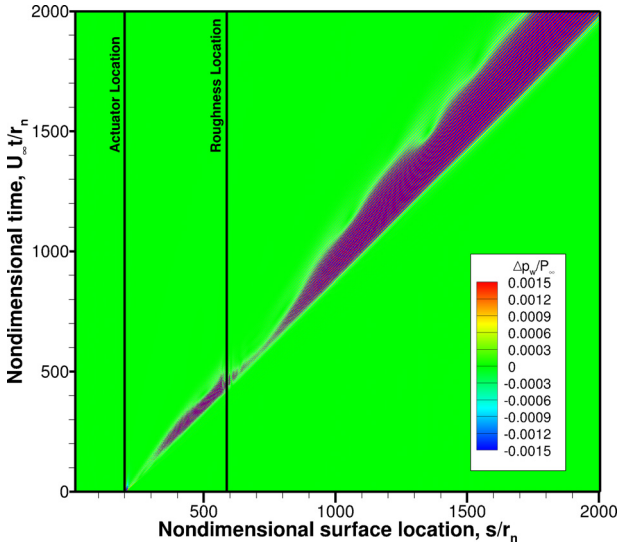

FIG. 10. The wave packet's surface pressure perturbation contours for all time with a single roughness strips. Contour levels are clipped to emphasize the wave's structure and trajectories; max $|\Delta p_w/P_\infty| = 0.0262$.

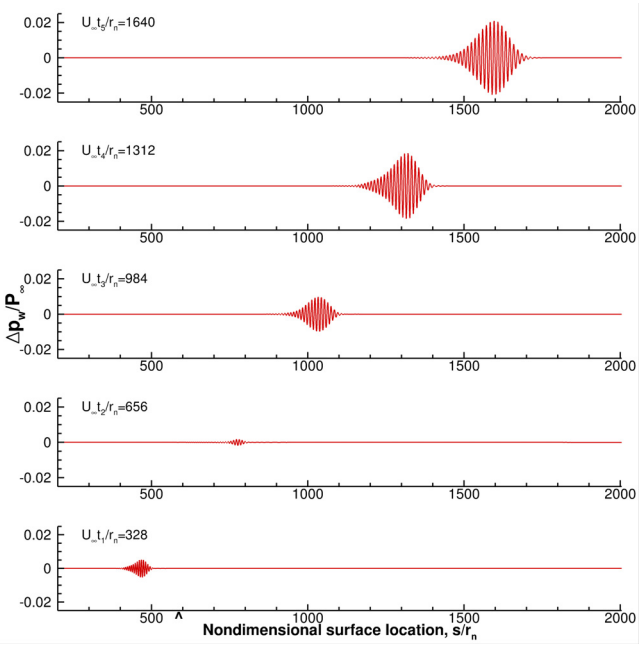

FIG. 11. Propagation of wave packet along the cone surface with a single roughness strip. The instantaneous pressure is plotted at five equal nondimensional time intervals of $U_\infty \Delta t/r_n = 328$ ($\Delta t = 0.15$ ms). Roughness strip location is noted by the arrow on the bottom plot.

wave maintains its appearance as a coherent wave packet with no additional modulation. So in brief, the roughness strip successfully dampens the unstable wave packet but does not stabilize it, as seen by its later re-growth.

3. Roughness array configuration

We now come to the unsteady results for the roughness array. The idea behind the roughness array is to use multiple roughness strips to continually attenuate the second mode instability. As specified in Table IV, six strips are utilized and spaced $20\delta_{99}$ thicknesses apart. The same blowing-suction actuator location and pulse parameters listed in Table II are added to the roughness array's steady-state solution. Figure 12 shows the axisymmetric view of the wave packet as it approaches the roughness array of six elements. Initially, the wave packet is fully formed and contains the rope-like structures indicative of the second mode instability. As the disturbance passes over the first strip in the array [Fig. 12(a)], part of the disturbance is swept up into the flow above the boundary layer. The part of the disturbance wave in the boundary layer is left visibly weaker by the first roughness strip. These flow behaviors are consistent with the single roughness configuration's unsteady results. By the second and third strips in the array [Fig. 12(b)], the wave packet is barely visible. Meanwhile, the oscillations in the inviscid flow behind the bow shock proceed to dissipate. Thus far, the disturbance pressure results in Fig. 12(b) show that the first half of the array is effective at damping the second mode instability.

The wave packet's propagation over the remaining strips in the array continues in Fig. 13. By the fourth strip in the six strip array, the weakened wave packet is spread out over the array [Fig. 13(a)], with part of the packet passing over the fourth strip and another part in between the fourth and fifth strips. The packet shows some signs of amplification as it approaches the fourth strip. The same behavior can be seen near the fifth and sixth strips [Fig. 13(b)], where the packet is wider than the distance between the strips. The packet widening, due to wave dispersion, causes different sections of the wave to be amplified, attenuated, and amplified again simultaneously. Meanwhile, parts of the wave are transported away into the inviscid layer as it passes

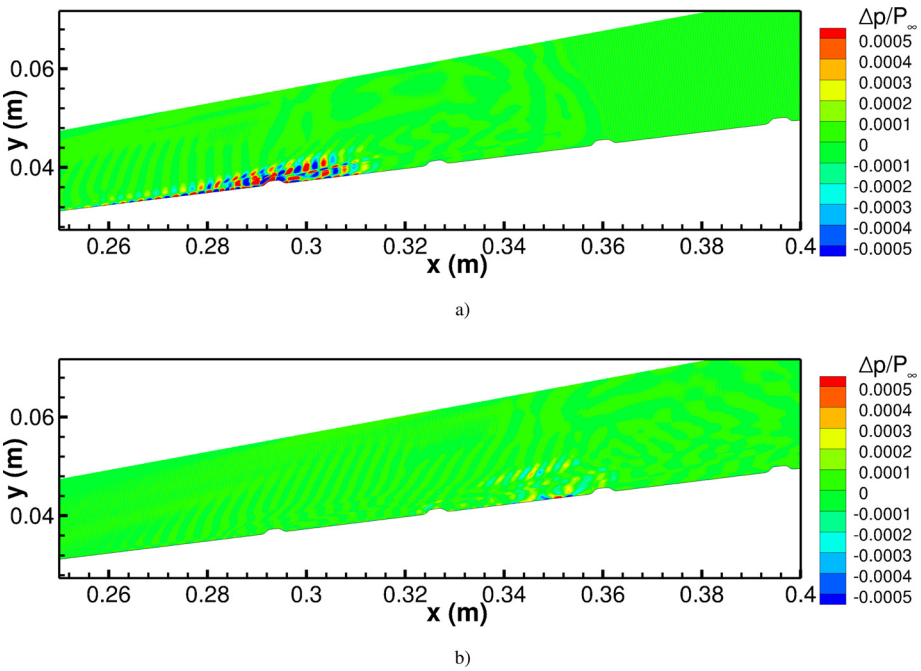

FIG. 12. (a) Instantaneous pressure perturbation contours of the wave packet as it traverses the first roughness strip. (b) The wave packet is significantly damped by the second roughness strip. Contour levels are clipped to emphasize the disturbance's structure.

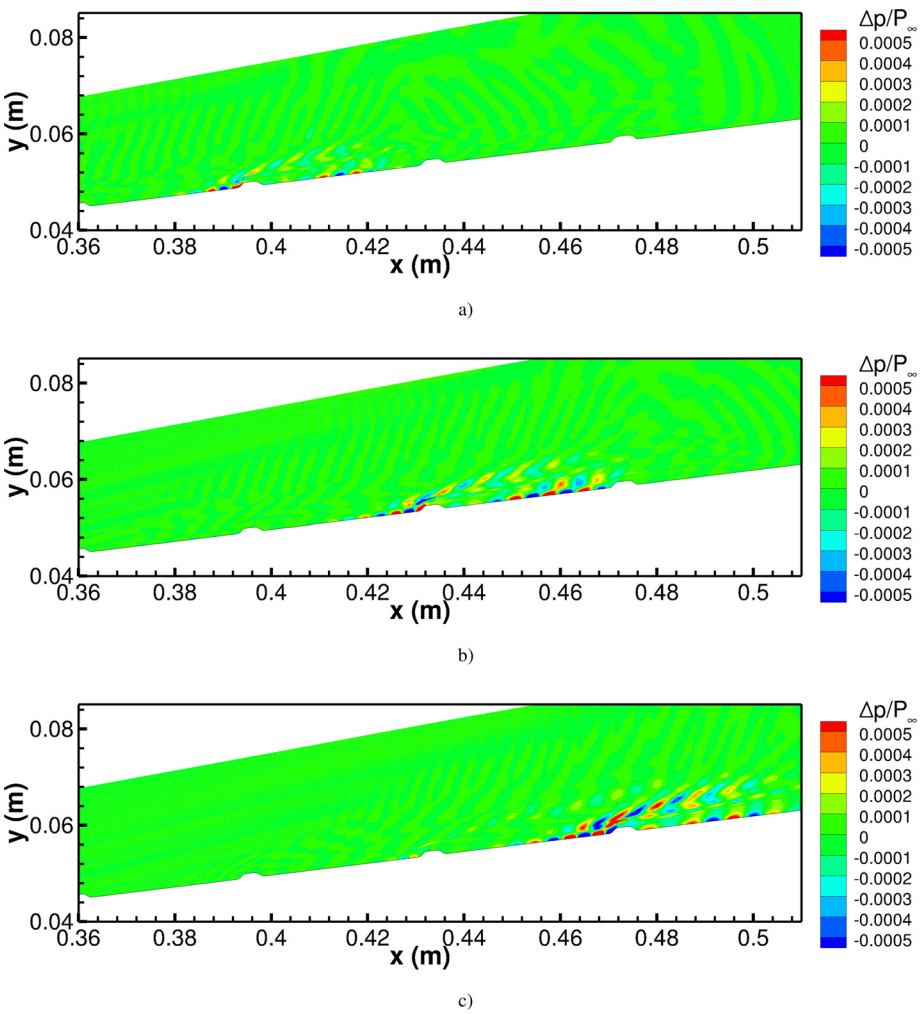

FIG. 13. Continuation of the instantaneous perturbation contours for the last four strips in the six strip array. (a) The wave packet remains significantly damped by the fourth strip. (b) The wave packet is spread across the fifth and sixth strips. (c) The wave packet departs the roughness array at the sixth strip.

over each roughness strip. The sixth and last strip in the array [Fig. 13(c)] shows upstream amplification near the strip and downstream attenuation. Unlike the upstream roughness strips, the perturbations pushed into the inviscid layer appear stronger. This could be due to changes in the boundary layer height caused by the preceding roughness strips. Downstream of the last element, the oscillations appear weaker but are already growing in amplitude. Overall, the roughness array successfully damps the second mode instability, but in doing so, it undergoes cycles of amplification and damping along with the shedding of disturbance energy into the flow above the boundary layer. The attenuation result is consistent with Fong *et al.*'s[10] previous findings for a flat plate.

Focusing on the wave packet's long-term downstream behavior, Fig. 14 shows the packet as it propagates away from the roughness array. The wave packet is clearly damped and barely visible within the boundary layer [Fig. 14(a)]; likewise, the oscillations in the flow behind the bow shock appear to dissipate. This result is consistent with the previous studies performed on a flat plate in Refs. 9–11, 33, and 42. As the wave packet propagates farther downstream, it grows rapidly in amplitude. By Fig. 14(b), the packet is proportionally as strong as it was upstream of the array and continues to grow farther downstream. While research on the roughness effect has already established that roughness elements amplify the lower downstream frequencies, this downstream evolution is eye-opening. The sudden re-growth of the wave packet shows that, although the roughness array delayed amplification of the second mode instability, it also destabilized the boundary layer. The result indicates that the passive boundary layer control strategy must be applied to the whole length of the cone to keep the second mode instability attenuated.

The wave packet's surface pressure perturbation along the cone's surface for the whole unsteady simulation is presented in Fig. 15. The contour plot clearly shows that the roughness array attenuates the wave packet around the array and downstream of the array. Except for a few patches in between the roughness strips where there is intermittent growth, the waves are damped to the point where they are no longer visible. This is a clear result of the roughness effect phenomenon. Additionally, the general shape of the wave fan is still present: with a slower wave trajectories on the left and faster trajectories on the right. Importantly however, downstream of the array, the wave packet begins to grow again, reaching a much higher maximum disturbance pressure ratio of 0.105. Overall, the array manages to attenuate the disturbance

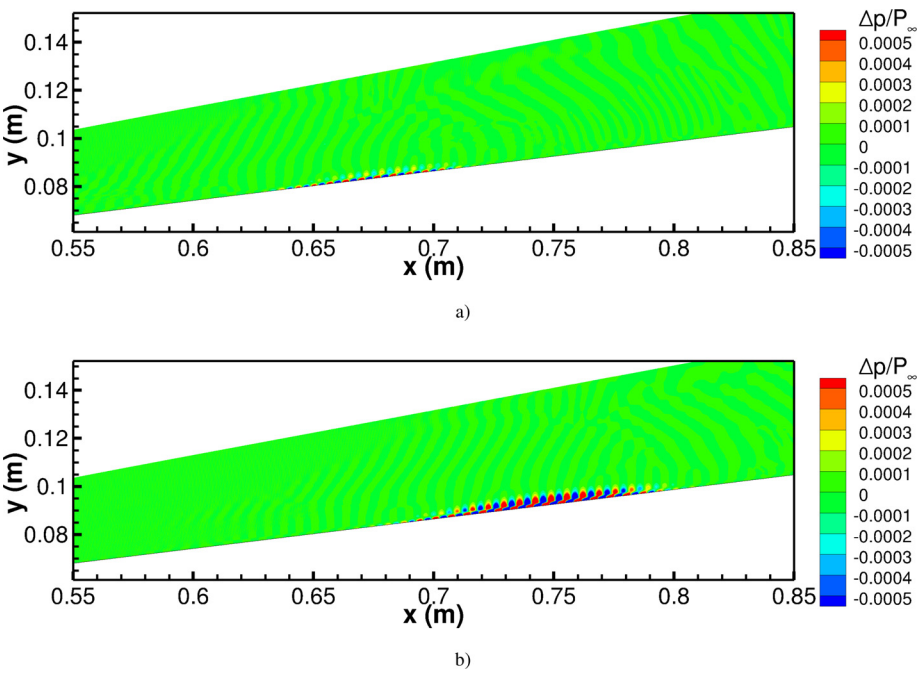

FIG. 14. Continuation of the instantaneous pressure perturbation contours for the region downstream of the roughness array. (a) The wave packet is significantly damped. (b) The wave packet shows significant downstream amplitude growth. Contour levels are clipped to emphasize the disturbance.

for a distance of $\Delta s/r_n = 800$–900 (0.4–0.45 m); however, the increased maximum pressure ratio clearly shows that the array is destabilizing to the boundary layer long term. No such result has been observed in the literature for flat plate simulations and could be a significant result.

For a closer look the wave's attenuation and amplification, instantaneous pressure waves at discrete time intervals are presented in Fig. 16. The pressure waves are taken at the same $U_\infty \Delta t/r_n = 328$ ($\Delta t = 0.15$ ms) intervals as the single roughness case. At $U_\infty t_1/r_n = 328$, the wave packet is upstream of the roughness array, as indicated by the arrows on the bottom of the plot. The six roughness strips in the array then attenuate the wave packet significantly at

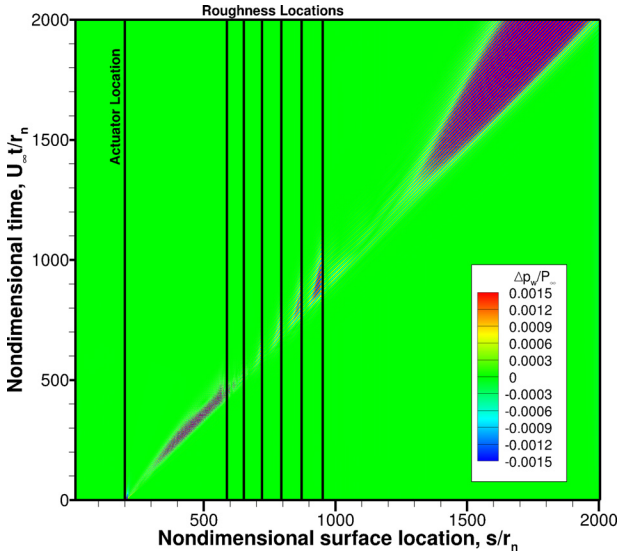

FIG. 15. The wave packet's surface pressure perturbation contours for all time with an array of six roughness strips. Contour levels are clipped to emphasize the wave's structure and trajectories; max $|\Delta p_w/P_\infty| = 0.105$.

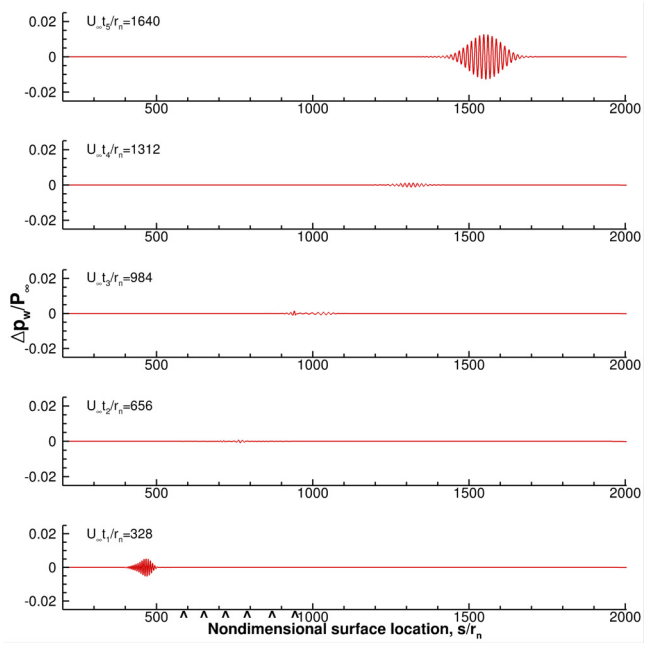

FIG. 16. Propagation of surface pressure wave along the cone surface with roughness array. The instantaneous pressure ratio is plotted at five equal nondimensional time intervals of $U_\infty \Delta t/r_n = 328$ ($\Delta t = 0.15$ ms). Roughness strip locations are noted on the bottom plot.

$U_\infty t/r_n = 656$, 984, and 1312. In general, the wave packet is attenuated by a factor of three or more. By $U_\infty t_4/r_n = 1312$, the wave packet is downstream of the last strip and already starting to grow in amplitude. At $U_\infty t_5/r_n = 1640$, the wave packet has grown significantly over the short distance. The wave packet is two-thirds the amplitude of the single roughness case wave packet in Fig. 11 at the same instant in time. This behavior indicates that although the disturbance is attenuated for longer with the array than a single strip, the array could ultimately act to destabilize the boundary layer.

To summarize briefly, the unsteady DNS results in this section conform qualitatively to the flat plate results found in the literature. Both the single roughness case and roughness array case are able to attenuate unstable wave packets using the roughness effect. However, the re-growth of the wave packet downstream of the roughness configurations is a new result not previously seen in the literature and could have important ramifications in applying a transition-delaying control strategy using the roughness effect. What remains to be investigated is to quantify which frequency ranges are attenuated/amplified and if the synchronization location criterion is still valid in conical flows. This can be achieved with a Fourier decomposition of the pressure perturbation data, which provides a frequency spectrum for the wave packet. The Fourier decomposition of the smooth cone case, single roughness strip case, and roughness array case can be found in Sec. III D.

D. Fourier decomposition of unsteady results

Since the wave packet is comprised of many frequencies, it is possible to use Fourier decomposition to obtain its power spectrum density (PSD). The decomposition provides insight into the growth and decay of individual frequencies and is more readily compared with LST results. The decomposition also provides a means to evaluate the validity of the synchronization location criterion, ultimately identifying which frequency ranges are attenuated/amplified by the roughness location.

The unsteady wall pressure perturbation data featured in Figs. 7, 10, and 15 are used to obtain the wave packet's PSD for each of the cases being studied. The PSD for the smooth surface cone and both roughness configurations are featured in Fig. 17. In addition to the spectra, the neutral stability curve for mode S obtained from LST is plotted in each subfigure. The subfigures show excellent agreement between each spectra and branch II of the neutral stability curve. Since growth rates are unstable in between branches I and II, instabilities are expected to grow within the neutral stability curve and decay beyond branch II. As Fig. 17(a) illustrates, for a fixed frequency, the amplitude grows to the left of branch II and begins to dampen immediately to the right. Branch II nearly perfectly delineates the region between positive and negative spectral pressure growth along the cone. This close agreement is important to note because LST and Fourier decomposition are two separate and independent methods of analysis and their close agreement helps to verify the results.

Moreover, the pressure spectrum contours in Fig. 17(a) show that the frequency content of the second mode instability varies as it propagates downstream. Higher frequencies increase in amplitude before damping out, while lower frequencies, which initially have no amplitude, gradually grow downstream. This result shows that the instability contains only a small range of frequencies at any given location, with the frequency content shifting to lower frequencies. Lower unstable frequencies also remain in the boundary layer longer than higher unstable frequencies, which allows instabilities with small growth rates to reach high amplitudes. As such, lower frequencies pose a greater risk of causing laminar–turbulent transition.

Moving on to the Fourier analysis of the roughness configurations, Fig. 17(b) contains the pressure spectrum for the cone with a single roughness strip. The single roughness strip alters the spectrum significantly: pressure amplitudes between 206 and 249 kHz and ranging between $s/r_n = 596$ and 864 (0.298 and 0.432 m) are highly attenuated. While unstable frequencies lower than 206 kHz see an increase in amplitude. Crucially, the amplified frequency range is below the roughness synchronization location frequency of 208 kHz as expected per the roughness effect phenomenon. This important result shows that the synchronization location criterion investigated by Fong *et al.*[10,11,33,42,44] in planar flows is also valid in conical flows.

The remaining pressure spectrum contours in Fig. 17(b) follow the smooth surface spectrum's general shape, which grows and decays with respect to branch II of the neutral curve. Furthermore, the N-factor analysis and previous experimental[28] results indicate that a frequency of 240 kHz is expected to start intermittent turbulence around $s/r_n = 680$ (0.340 m). Figure 17(b) shows that the 240 kHz target frequency is sufficiently attenuated by the roughness strip, which is the ultimate goal of the passive boundary layer control method. At present, however, there is no way to accurately determine how far transition would be delayed by the roughness strip without a fully turbulent simulation or an experiment. However, by comparing the smooth and single roughness strip pressure spectra contour values, we estimate that second mode growth could be delayed by as much as $\Delta s/r_n = 184$ (9.2 cm) to $s/r_n = 864$ (0.432 m). Unfortunately, it is clear from the amplified spectrum that the roughness strip destabilizes the boundary layer downstream of this point and will inevitably lead to transition. Thus, the 1 m cone provides clear evidence that the single roughness strip can delay the growth of the second mode instability for some distance but ultimately does not stabilize the boundary layer.

The unavoidable destabilization of the boundary layer, however, can be remedied by using multiple roughness strips. The PSD in Fig. 17(c) shows that the roughness array has altered the spectrum even further than the single roughness strip. Frequencies between 156 and 249 kHz are attenuated, while unstable frequencies lower than 156 kHz see an increase in amplitude. The cone surface between $s/r_n = 596$ and 1354 (0.298 and 0.677 m) has also been cleared of the second mode instability. As with the single roughness strip, the array has significantly attenuated the 240 kHz target frequency responsible for transition onset, and with the use of multiple strips, we can estimate that second mode growth could be delayed by at much as $\Delta s/r_n = 674$ (33.7 cm) to $s/r_n = 1354$ (0.677 m). This result clearly shows that the roughness array can delay second mode instability growth downstream over longer distances. However, once the array ends, frequencies lower than the synchronization frequency of the last strip (164 kHz) are amplified significantly compared to the no roughness case. This amplification undoubtedly makes transition inevitable. Thus, the far downstream behavior of the second mode instability on the 1 m cone clearly shows that the roughness effect ultimately amplifies the instability. However, the roughness array result also demonstrates that the addition of successive strips could further delay second mode amplitude growth.

Before proceeding further, we wish to emphasize the importance of the synchronization location in conical flows using the PSD.

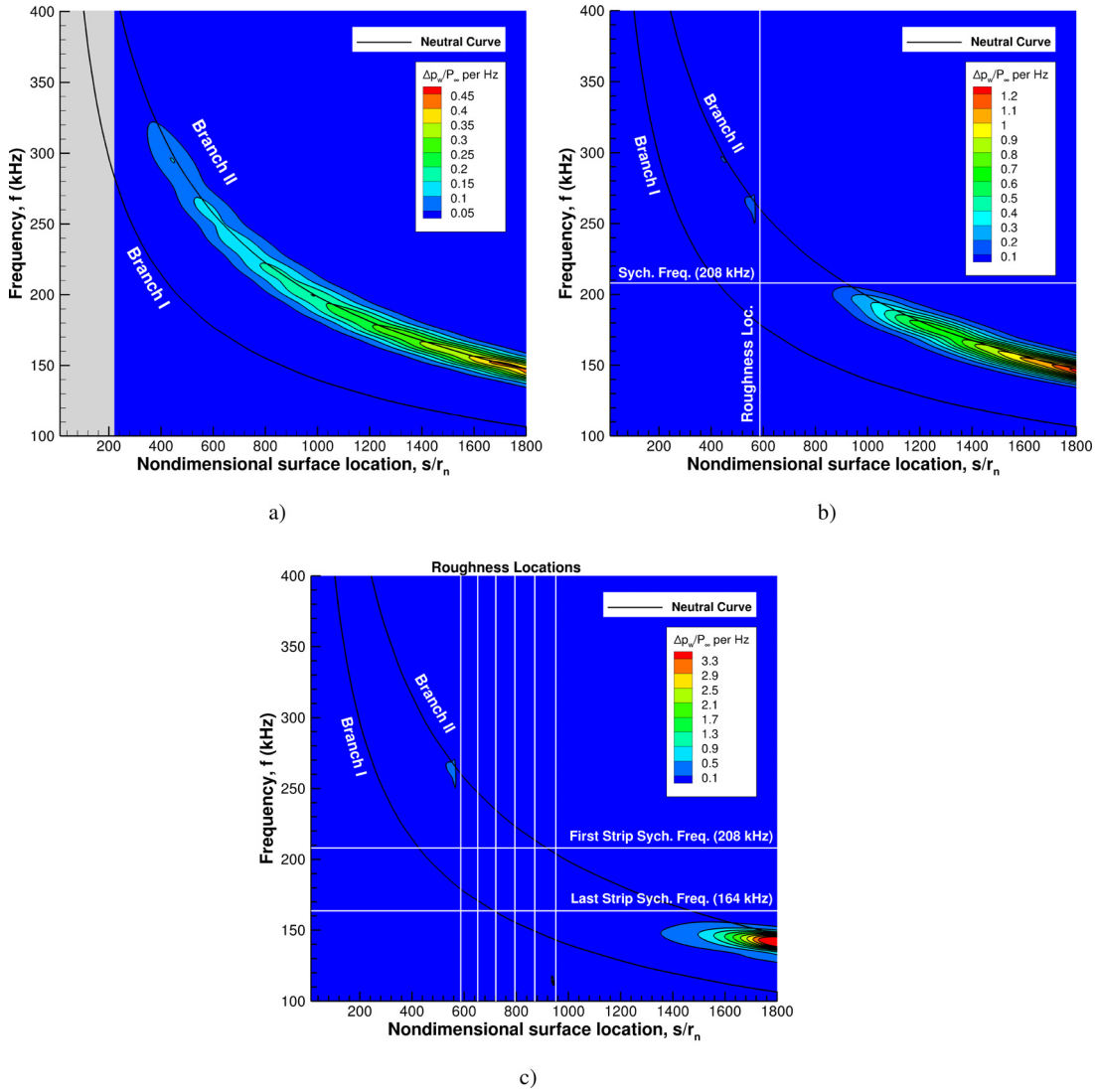

FIG. 17. Surface pressure perturbation spectra contours for the (a) smooth surface, (b) single roughness strip, and (c) roughness array of six strips. Roughness locations are denoted by white vertical lines. Branches I and II of the neutral stability curve are included for reference.

Figure 18 takes a closer look at the pressure spectrum contour for the single roughness configuration in the vicinity of the roughness strip. The figure contains several lines denoting features important to this paper. The first two are a solid vertical line denoting the roughness strip location and a white horizontal dashed line denoting the 208 kHz roughness synchronization frequency. As expected, these lines intersect on the synchronization curve. Following the dashed line downstream, we see some marginal attenuation, but more importantly, frequencies below the dashed line are amplified downstream and frequencies above it are attenuated. This is strong numerical evidence for the importance of the synchronization location and its role in the roughness effect phenomenon. Also included in Fig. 18 is a white horizontal dashed line denoting the 240 kHz target frequency for the onset of intermittent turbulence. Following the line downstream of the roughness location, we see an overall attenuation of the 240 kHz frequency, which is the desired outcome of the roughness strip design and the passive boundary layer control strategy. The last horizontal line in the figure is 179 kHz, which coincides with the branch I neutral point corresponding to the roughness strips location. There is some speculation that the branch I neutral point at the roughness location is responsible for determining which frequency ranges are attenuated or amplified. However, as the pressure spectrum shows, there is growth above the neutral point frequency. Demonstrating that the branch I neutral curve does not play a role in the roughness effect phenomenon.

Moving on, we can take a closer look at the surface pressure spectra results for both the single strip and the roughness array configurations by examining individual frequencies. Plotting select frequencies

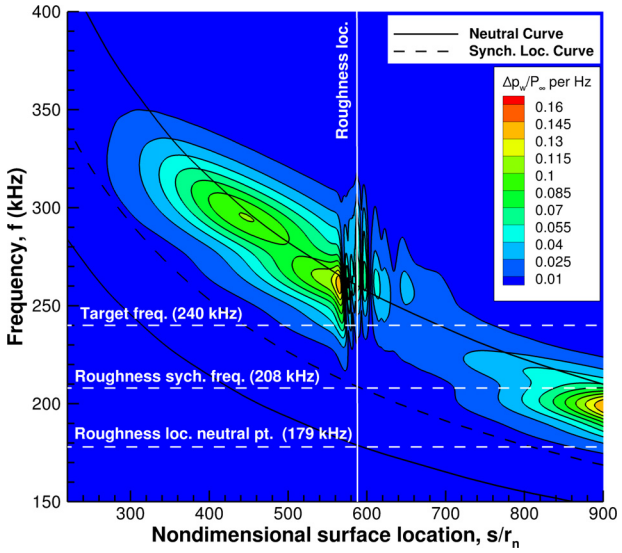

FIG. 18. Surface pressure perturbation spectra in the vicinity of the single roughness strip with several frequencies of interest.

reveals details about the pressure spectrum results that are otherwise obscured by discrete contour levels. For instance, the frequencies 275 and 250 kHz in Fig. 19(a) show growth upstream of the roughness strip and then attenuation downstream of it, but not before undergoing some damped oscillations immediately downstream of the roughness strip. The 225 kHz pressure perturbation spectrum shows some growth downstream of the strip, but the growth is inhibited by the roughness. This frequency is followed by the amplitudes for 200, 175, and 150 kHz, and all exhibit increased growth. This growth is expected as these frequencies are lower than the roughness strip synchronization frequency of 208 kHz.

Figure 19(b) looks at the same fixed frequencies for the roughness array surface pressure spectra results along with the frequency exhibiting the maximum downstream amplification. The frequencies 275 and 250 kHz are relatively unchanged, showing the same initial upstream growth, attenuation, and damped oscillations. However, the frequencies 225, 200, and 175 kHz differ from Fig. 19(a) and undergo complete attenuation with minor amplification in between each roughness strip in the array. Only the last two frequencies, 150 and 142 kHz, show significant growth. This growth is expected as these frequencies are lower than the synchronization frequency of 164 kHz for the last trip and the array. From the examination of individual frequencies for both roughness configurations, it is clear that the attenuation caused by the roughness effect phenomenon works by flat-lining the frequency's amplitude.

Since the objective of the passive boundary layer flow control strategy is to attenuate the second mode instability, it is advantageous to examine and compare the maximum pressure perturbation amplitude [max (p'_w/P_∞) per Hz] across the smooth and roughness configurations. Figure 20 compares the maximum pressure perturbation amplitude as a function of streamwise location. This figure makes the extent of the attenuation abundantly clear. For instance, both roughness configurations have the same max (p'_w/P_∞) per Hz as the smooth cone between the actuator at $s/r_n = 200$ (0.10 m) and the first roughness location at $s/r_n = 587.2$ (0.294 m). This shows that the roughness strips have very little upstream influence from their position. Downstream of the single roughness configuration, the roughness has effectively attenuated the maximum pressure perturbation up to $s/r_n = 928$ (0.464 m), where the single roughness plot intersects the plot for the smooth cone. Beyond this point, max (p'_w/P_∞) per Hz increases rapidly with a tremendous growth rate over the base flow, reaching a peak 2.8 times larger in magnitude. Likewise, the maximum pressure perturbation for the roughness array is effectively attenuated up to $s/r_n = 1462$ (0.731 m). At which point the growth rate for the roughness array maximum pressure perturbation explodes and

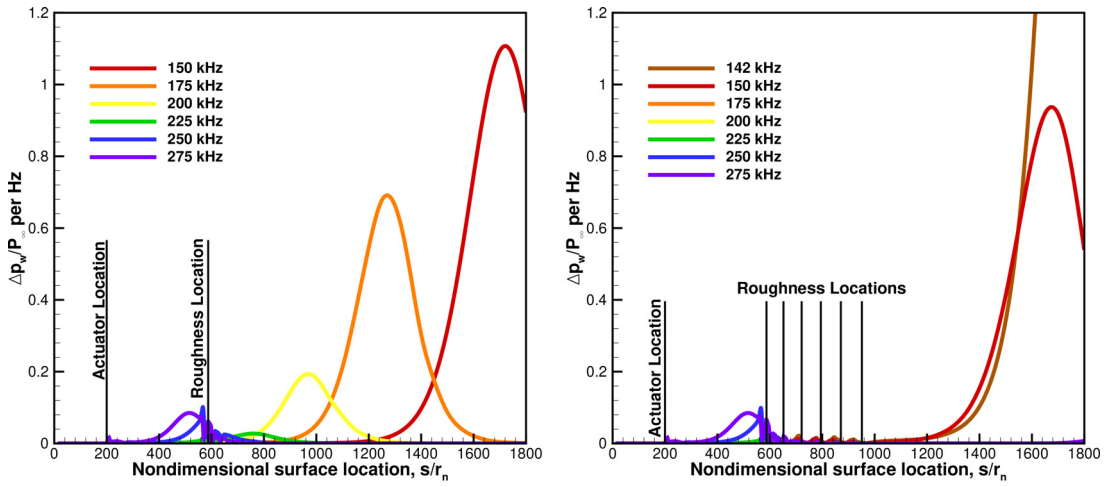

FIG. 19. Spatial evolution of pressure perturbation spectra at select frequencies for (a) a single roughness strip and (b) roughness array with six strips.

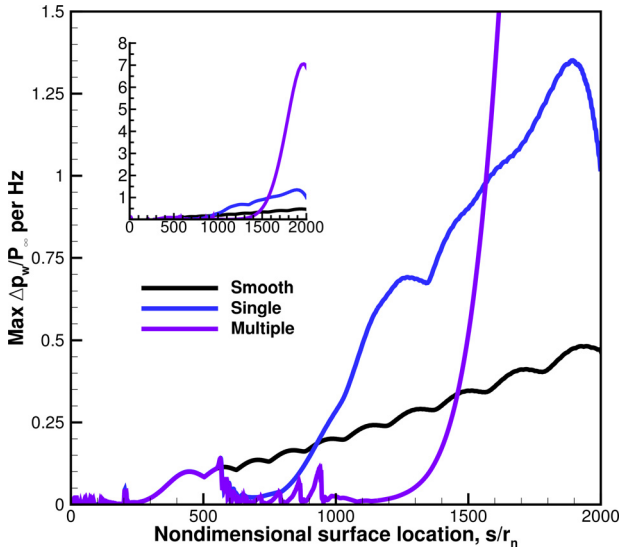

FIG. 20. Maximum pressure perturbation spectra, max($\Delta p_w/P_\infty$) per Hz, as a function of streamwise location for each of the cases under investigation.

reaches a peak 14.7 times higher than the smooth surface case. Figure 20 communicates quite effectively that the roughness effect can delay second mode growth but ultimately destabilizes the boundary layer.

Figure 21 compares the maximum pressure perturbation amplitude as a function of frequency. The figure clearly shows which frequencies are being attenuated and amplified. For frequencies higher than 272 kHz, no attenuation or amplification has taken place. This is the frequency range that grows and decays naturally before the unsteady wave packet reaches the roughness configurations. A narrow band between 251 and 272 kHz sees some slight amplification that can

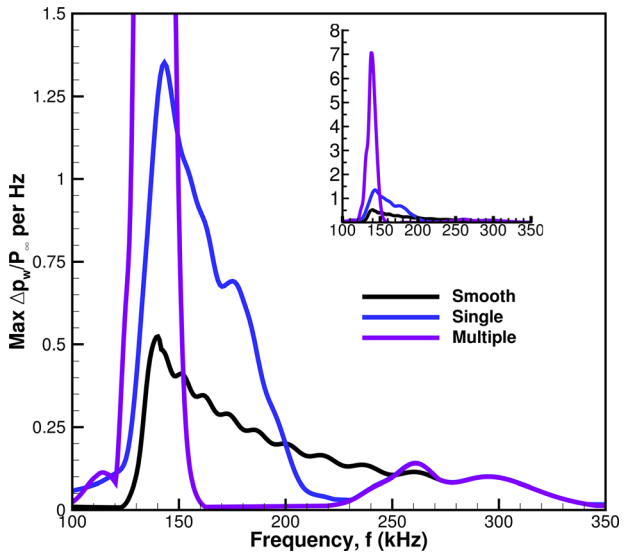

FIG. 21. Maximum pressure perturbation spectra, max($\Delta p_w/P_\infty$) per Hz, as a function of frequency for each of the cases under investigation.

be attributed to the decaying oscillations behind the first roughness location seen in Fig. 19. The range between 200 and 251 kHz for the single roughness strip is effectively attenuated. This range is the target range identified by the N-factor analysis to contain the 240 kHz frequency most likely to start intermittent turbulence. The successful attenuation of this range shows that the single roughness strip fulfilled its intended design. Frequencies below 200 kHz are amplified significantly, peaking around 142 kHz. The drop-off in amplitude for lower frequencies is due to the finite length of the cone and the unsteady wave packet exiting the computational domain. The result for the roughness array shows that frequencies between 152 and 251 kHz are effectively attenuated; in fact, most of the range is essentially flat, which is the goal of the control strategy. However, around 161 kHz, amplitudes grow tremendously fast, reaching a peak around 138 kHz as seen in the inset plot.

Both roughness configurations show an interesting behavior of the roughness effect phenomenon. It would appear that the surface roughness does not dampen or dissipate the second mode instability as initially thought but instead transfers the disturbance energy from higher frequencies to an increasingly narrow band of lower frequencies.

Finally, an interesting detail in the smooth cone maximum pressure perturbation amplitude in Figs. 20 and 21 is the undulations in both the positional and frequency plots. Presumably, linear growth of the instability would not cause the curve to undulate. This issue is addressed in great detail in Ref. 45. In brief, it results from primary and secondary wave interference brought on by forcing caused by the blowing-suction actuator and its proximity to the neutral curve.

IV. SUMMARY

This paper presents a computational and theoretical investigation on the ability of isolated surface roughness configurations to attenuate second mode instability growth on a Mach 8 hypersonic blunt cone. The DNS code solves the conservative three-dimensional Navier–Stokes equations under a perfect gas assumption. The axisymmetric surface roughness elements are applied to the cone surface using a body-fitted grid over an analytical shape. This approach, along with shock-fitting, allows for a uniform fifth-order global accuracy throughout the domain. Unsteady results are produced using a blowing-suction actuator, which produces a Gaussian broadband pulse to excite Mack's second modal instability.

This investigation is the first time the passive boundary layer control strategy patented by Zong *et al.*[12] has been simulated on a blunt straight cone. Previous computational investigations of the transition-delaying roughness are limited to flat plate simulations. Previous investigations of surface roughness on a cone were either not investigating the roughness effect phenomenon, not using high-order methods, or not including the effect of the bow shock in their simulations. The present investigation's approach of combining high-order finite difference methods with shock-fitting techniques to simulate transition-delaying roughness makes this paper unique.

The paper investigates two configurations of transition-delaying roughness, a single roughness strip and an array of successive roughness strips, as well as a smooth surface comparison case. The passive laminar boundary layer control strategy is used to design both configurations. The strategy entails computing the flow's steady-state, computing its N-factors, identifying the frequency likely to start

laminar–turbulent transition, finding its synchronization location, and then dimensionalizing a roughness strip to the boundary layer's proportions at that location.

Linear stability theory (LST) and Fourier decomposition (FFT) are the predominant methods used to analyze the steady-state and unsteady simulations in this paper. LST is used to compute the growth rates for the N-factor calculations and perform the steady-state stability analysis, including modal phase speed and neutral curve results. A Gaussian pulse is used to perturb the boundary layer to a wide range of frequencies and then analyzed with Fourier decomposition to study the disturbance spectra produced by the pulse. Where the two methods overlap, they produce consistent results—for instance, the smooth cone surface pressure perturbation spectrum shows close agreement with the onset of modal growth and decay as predicted by the neutral curve.

Prior to this investigation, there was no guarantee that the synchronization location hypothesis in a planar flow would hold in a conical flow. The findings in this paper reinforce the role of the synchronization location in attenuating the second mode instability with isolated surface roughness—mainly that roughness elements shorter than the local boundary layer height can attenuate frequencies above the synchronization frequency while amplifying those below it. The simulations' findings are consistent with Fong *et al.*'s[10,11,33,42,44] findings for a hypersonic flat plate.

However, one instance in which the cone simulation differs remarkably from flat plate simulations is that the cone's downstream separation zone behind the roughness separation zone is significantly smaller. The reason for this was not extensively investigated but could be because of the cone's axisymmetry and the cone's surface inclination to the flow. The result is notable because the downstream separation zone has been proposed as a damping mechanism. However, the attenuation of the second mode instability on a cone is comparable to the attenuation on a flat plate, despite the separation zone's diminutive size, suggesting it is not the source of the damping. At this time, however, the downstream separation zone's size is a cursory observation, but its role as a damping mechanism merits further investigation.

The investigation also confirms that the second mode instability's attenuation results from the element's proximity to the synchronization location and not due to its proximity with the branch I neutral point. A criticism of the control strategy is that the coincidence of the roughness' location and the branch I neutral frequency determines the cutoff between attenuated and amplified frequencies. However, Fourier decomposition of the unsteady wave packet for the single roughness strip shows that the branch I neutral frequency, which is lower than the synchronization frequency, is contained in the range of amplified frequencies. This amplification indicates that the branch I neutral point does not determine the cutoff frequency for the roughness effect phenomenon.

Previous computational studies on the roughness effect focused on a Mach 5.92 flow regime. This regime is close to where hypersonic flow is generally agreed to start and contains both first and second mode instabilities. The Mach 8 flow in the present investigation extends roughness effect research to more relevant Mach numbers where second mode instabilities dominate. The ability of the roughness array to attenuate the instability at Mach 8 shows that the control strategy works in higher Mach flows and is also insensitive to the strength of the instability.

The 1 m cone in this investigation provides new insight into the roughness effect and the long-term feasibility of the passive laminar boundary layer control strategy. The single roughness strip and roughness array configurations looked at the long-term downstream growth of unattenuated second mode frequencies. Prior to the investigation, it was unknown if the unattenuated frequencies would resume growth at their normal growth rate or if it would be accelerated. The results are insightful; maximum pressure perturbation PSD, as a function of surface location, shows that the PSD is many times larger for the simulations with surface roughness than the base simulation without roughness. The PSD for a single roughness reaches a peak $\Delta p_w/P_\infty$ per Hz that is 2.8 times larger than the base case. Likewise, the PSD for the roughness array reaches a $\Delta p_w/P_\infty$ per Hz that is 14.7 times higher than the base case. The same results show that the control strategy is very effective at attenuating their targeted frequencies, but if the strategy is not carried out to the end of the cone, the unattenuated frequencies will grow significantly. Thus, for the control strategy to be effective, it must be applied to the entire length of the cone.

Furthermore, when looking at the maximum pressure perturbation PSD as a function of frequency, we see that the control strategy concentrates the disturbance into a narrowing band of amplified frequencies. This narrowing suggests that the roughness effect phenomenon or control strategy does not necessarily dampen or dissipate the second mode instability but instead transfers disturbance energy from higher frequencies to lower frequencies. While there is some dissipation into the inviscid layer as the wave packet travels over the roughness strip, it appears most of the energy is transferred into these lower frequencies. Again the results indicate that the control strategy needs to be judiciously applied to the entire cone frustum to be effective.

At this point, there are many directions in which future work can go. For instance, the roughness effect's ability to attenuate oblique wave instabilities, such as Mack's first mode instability, has not been adequately studied. The roughness effect has also not been adequately studied in flow fields where modes S and F couple but do not intersect with a clearly defined synchronization point. Moreover, only 2D and axisymmetric simulations of transition-delaying roughness have been explored; the next logical step is to extend the investigation to include 3D isolated roughness.

Finally, there are realizable applications of the passive boundary layer control strategy. The first is a reduction in thermal protection system (TPS) weight; by delaying turbulent transition, the airframe experiences a reduced heat flux and requires less TPS. A second application is around complex surface geometry, such as control surface joints, where traditional TPS is challenging to apply. A third application is around surface-mounted instrumentation or above subsurface electronic hardware that traditional TPS would otherwise inhibit. Moreover, traditional TPS techniques can be used downstream of these applications to mitigate the turbulent heat transfer caused by the control strategy's destabilization of the boundary layer. In order to know if any of these proposed applications are feasible, more research on the roughness effect phenomenon is needed.

ACKNOWLEDGMENTS

This work is sponsored by the Air Force Office of Scientific Research, USAF, under AFOSR Grants No. FA9550-15-1-0268, monitored by Dr. Ivett Leyva. The computations are mainly run on

XSEDE resources provided by Texas Advanced Computing Center (TACC) and San Diego Supercomputer Center (SDSC) under Grant No. TG-ASC090076 supported by the National Science Foundation. The views and conclusions contained herein are those of the author and should not be interpreted as necessarily representing the official policies or endorsements either expressed or implied, of the Air Force Office of Scientific Research or the U.S. Government. Dr. Katya Casper is acknowledged for her collaboration and agreeing to run roughness experiments, validative, explorative or otherwise, in Sandia National Labs Hypersonic Wind Tunnel facility.

AUTHOR DECLARATIONS

Conflict of Interest

The authors have no conflicts to disclose.

Author Contributions

Christopher Louis Haley: Conceptualization (lead); Data curation (lead); Formal analysis (lead); Investigation (lead); Methodology (lead); Software (lead); Visualization (lead); Writing – original draft (lead); Writing – review & editing (lead). **Xiaolin Zhong:** Conceptualization (equal); Funding acquisition (lead); Methodology (supporting); Project administration (equal); Resources (equal); Software (supporting); Supervision (lead); Writing – review & editing (supporting).

DATA AVAILABILITY

The data that support the findings of this study are available from the corresponding author upon reasonable request.

REFERENCES

[1]X. Zhong and X. Wang, "Direct numerical simulation on the receptivity, instability, and transition of hypersonic boundary layers," Annu. Rev. Fluid Mech. **44**, 527–561 (2012).
[2]W. H. Dorrance, *Viscous Hypersonic Flow: Theory of Reacting and Hypersonic Boundary Layers* (Dover Publications, Inc., Mineola, NY, 2017).
[3]W. S. Saric, H. L. Reed, and E. J. Kerschen, "Boundary-layer receptivity to freestream disturbances," Annu. Rev. Fluid Mech. **34**, 291–319 (2002).
[4]M. V. Morkovin, E. Reshotko, and T. Herbert, "Transition in open flow systems—A reassessment," Bull. Am. Phys. Soc. **39**, 1882 (1994).
[5]S. P. Schneider, "Effects of roughness on hypersonic boundary-layer transition," J. Spacecr. Rockets **45**, 193–209 (2008).
[6]S. P. Schneider, "Summary of hypersonic boundary-layer transition experiments on blunt bodies with roughness," J. Spacecr. Rockets **45**, 1090–1105 (2008).
[7]E. Reshotko and A. Tumin, "Role of transient growth in roughness-induced transition," AIAA J. **42**, 766–770 (2004).
[8]P. Paredes, M. M. Choudhari, F. Li, J. S. Jewell, R. L. Kimmel, E. C. Marineau, and G. Grossir, "Nose-tip bluntness effects on transition at hypersonic speeds," J. Spacecr. Rockets **56**, 369–387 (2019).
[9]L. Duan, X. Wang, and X. Zhong, "A high-order cut-cell method for numerical simulation of hypersonic boundary-layer instability with surface roughness," J. Comput. Phys. **229**, 7207–7237 (2010).
[10]K. D. Fong, X. Wang, and X. Zhong, "Numerical simulation of roughness effect on the stability of a hypersonic boundary layer," Comput. Fluids **96**, 350–367 (2014).
[11]D. Fong, X. Wang, and X. Zhong, "Finite roughness effect on modal growth of a hypersonic boundary layer," AIAA Paper No. 2012-1086, 2012.
[12]X. Zhong, K. D. Fong, and X. Wang, "Hypersonic laminar flow control," Patent No. US 10,071,798 B2 (11 Sept. 2018).
[13]C. S. James, "Boundary-layer transition on hollow cylinders in supersonic free flight as affected by Mach number and a screwthread type of surface roughness," Report No. NASA-MEMO-1-20-59A (1959), see https://ntrs.nasa.gov/citations/19980228370.
[14]P. F. Holloway and J. R. Sterrett, "Effect of controlled surface roughness on boundary layer transition and heat transfer at Mach numbers of 4.8 and 6.0," Report No. NASA-TN-D-2054 (1964).
[15]K. Fujii, "Experiment of the two-dimensional roughness effect on hypersonic boundary-layer transition," J. Spacecr. Rockets **43**, 731–738 (2006).
[16]B. C. Chynoweth, C. A. C. Ward, R. T. Greenwood, G. R. McKiernan, R. A. Fisher, and S. P. Schneider, "Measuring transition and instabilities in a Mach 6 hypersonic quiet wind tunnel," AIAA Paper No. 2014-2643, 2014.
[17]K. D. Fong, X. Wang, Y. Huang, X. Zhong, G. R. McKiernan, R. A. Fisher, and S. P. Schneider, "Second mode suppression in hypersonic boundary layer by roughness: Design and experiments," AIAA J. **53**, 1–6 (2015).
[18]Q. Tang, Y. Zhu, X. Chen, and C. Lee, "Development of second-mode instability in a Mach 6 flat plate boundary layer with two-dimensional roughness," Phys. Fluids **27**, 064105 (2015).
[19]C. H. Mortensen and X. Zhong, "Real-gas and surface-ablation effects on hypersonic boundary-layer instability over a blunt cone," AIAA J. **54**, 980–919 (2016).
[20]A. Sescu, J. Sawaya, V. Sassanis, and M. R. Visbal, "Study of the effect of two-dimensional wall non-uniformities on high-speed boundary layers," AIAA Paper No. 2017-4511, 2017.
[21]M. Dong, Y. Liu, and X. Wu, "Receptivity of inviscid modes in supersonic boundary layers due to scattering of free-stream sound by localised wall roughness," J. Fluid Mech. **896**, A23 (2020).
[22]M. Dong and L. Zhao, "An asymptotic theory of the roughness impact on inviscid Mack modes in supersonic/hypersonic boundary layers," J. Fluid Mech. **913**, A22 (2021).
[23]D. C. Berridge, C. Yam, G. McKiernan, D. R. Eby, C. L. Carpenter, and J. S. Jewell, "Roughness effects on the crossflow instability on the HIFiRE-5 geometry," AIAA Paper No. 2022-1211, 2022.
[24]L. N. Wagner, S. P. Schneider, and J. S. Jewell, "Streamwise vortices from controlled roughnesses on a cone-cylinder-flare at Mach 6," AIAA Paper No. 2022-1671, 2022.
[25]P. Paredes, M. M. Choudhari, F. Li, J. S. Jewell, and R. L. Kimmel, "Nonmodal growth of traveling waves on blunt cones at hypersonic speeds," AIAA J. **57**, 4738–4749 (2019).
[26]P. Paredes, A. Scholten, M. M. Choudhari, F. Li, B. N. Price, and J. S. Jewell, "Combined bluntness and roughness effects on cones at hypersonic speeds," AIAA Paper No. 2022-3340, 2022.
[27]X. Zhong, "High-order finite-difference schemes for numerical simulation of hypersonic boundary-layer transition," J. Comput. Phys. **144**, 662–709 (1998).
[28]K. M. Casper, S. J. Beresh, J. F. Henfling, R. W. Spillers, B. O. M. Pruett, and S. P. Schneider, "Hypersonic wind-tunnel measurements of boundary-layer transition on a slender cone," AIAA J. **54**, 1250–1263 (2016).
[29]W. Sutherland, "LII. The viscosity of gases and molecular force," London, Edinburgh, Dublin Philos. Mag. J. Sci. **36**, 507–531 (1893).
[30]Y. Huang and X. Zhong, "Numerical study of hypersonic boundary-layer receptivity with freestream hotspot perturbations," AIAA J. **52**, 1–21 (2014).
[31]J. Lei and X. Zhong, "Linear stability analysis of nose bluntness effects on hypersonic boundary layer transition," J. Spacecr. Rockets **49**, 24–37 (2012).
[32]J. Williamson, "Low-storage Runge-Kutta schemes," J. Comput. Phys. **35**, 48–56 (1980).
[33]K. D. Fong, X. Wang, and X. Zhong, "Parametric study on stabilization of hypersonic boundary layer waves using 2-D surface roughness," AIAA Paper No. 2015-0837, 2015.
[34]L. M. Mack, "Boundary layer linear stability theory," AGARD Technical Report No. 709 (1984).
[35]Y. Ma and X. Zhong, "Receptivity of a supersonic boundary layer over a flat plate—Part 1: Wave structures and interactions," J. Fluid Mech. **488**, 31–78 (2003).
[36]Y. Ma and X. Zhong, "Receptivity of a supersonic boundary layer over a flat plate—Part 2: Receptivity to free-stream sound," J. Fluid Mech. **488**, 79–121 (2003).

[37]M. R. Malik, "Numerical methods for hypersonic boundary layer stability," J. Comput. Phys. **86**, 376–413 (1990).
[38]C. P. Knisely and X. Zhong, "Sound radiation by supersonic unstable modes in hypersonic blunt cone boundary layers—I: Linear stability theory," Phys. Fluids **31**, 024103 (2019).
[39]C. P. Knisely and X. Zhong, "Sound radiation by supersonic unstable modes in hypersonic blunt cone boundary layers—II: Direct numerical simulation," Phys. Fluids **31**, 024104 (2019).
[40]J. L. van Ingen, "A suggested semi-empirical method for the calculation of the boundary layer transition region," Report No. VTH-74 (Delft University of Technology, Delft, The Netherlands, 1956).
[41]L. M. Mack, "Transition and laminar instability," Report No. NASA-CP-153203 (Jet Propulsion Laboratory, Pasadena, CA, 1977).
[42]K. D. Fong, X. Wang, and X. Zhong, "Stabilization of hypersonic boundary layer waves using 2-D surface roughness," AIAA Paper No. 2013-2985, 2013.
[43]A. Fedorov and A. Tumin, "High-speed boundary-layer instability: Old terminology and a new framework," AIAA J. **49**, 1647–1657 (2011).
[44]K. D. Fong and X. Zhong, "DNS and PSE study on the stabilization effect of hypersonic boundary layer waves using 2-D surface roughness," AIAA Paper No. 2016-3347, 2016.
[45]C. Haley and X. Zhong, "Supersonic mode in a low-enthalpy hypersonic flow over a cone and wave packet interference," Phys. Fluids **33**, 054104 (2021).